

1 Introduction

This supplement includes a description of the code, with a presentation of the features implemented followed by results of extensive benchmarks listed in Table 1, implemented to verify that the code solves correctly a large range of problems. Description and results of all benchmarks are shown in Section 10.

Feature	Benchmark	Section
Solver	Stokes flow	10.2
Markers advection	Zalesak disk Conservative Interpolation Velocity	10.3 10.4
Momentum equation	Poiseuille flow	10.5
	Instantaneous 2D sphere	10.6
	Rayleigh-Taylor experiment	10.7
	Falling block	10.8
Sticky air and free surface	2D Stokes sphere	10.9
	Stabilisation algorithm	10.10
	Topography relaxation	10.11
	Spontaneous subduction	10.12
Erosion and sedimentation	-	-
Non-linear visco-plasticity	Slab detachment	10.13
	Indenter	10.14
	Brick	10.15
Energy equation	Advection stabilisation	10.16
	Simple shear heating	10.17
	Shear and adiabatic heating	10.18
Energy + momentum	Mantle convection	10.19
	Viscoplastic mantle convection	10.20
	Thin layer entrainment	10.21
Phase changes and hydration	Hydrated sinking cylinder	10.22
Melting	Experimental melting curves	10.23

Table 1: List of benchmarks implemented for each feature of the code. Data of all benchmarks can be found at <https://github.com/aleregora/Benchmarks>

The code is written in Fortran90 and uses the finite element method (FEM) with quadrilateral $Q_1 \times P_0$ elements (continuous bilinear velocity and discontinuous constant pressure), associated with MUMPS¹ (Amestoy et al., 2001, 2019) that is a software package for solving systems of linear equations of the form $A \cdot x = b$, where A is a square sparse matrix, by means of a direct method. Since $Q_1 \times P_0$ elements do not satisfy Ladyzhenskaya, Babuska and Brezzi (LBB) stability condition (Donea and Huerta, 2003), elemental pressure is elaborated in post-processing to avoid spurious pressures by means of a double interpolation to smooth the pressure. Following this procedure, the elemental pressure is interpolated onto nodes and then back onto elements. After the smoothing procedure, the pressure field is calculated again on the nodes to be used in combination with the lithostatic pressure, which is calculated onto nodes. Correctness of the solution and performances of the solver in terms of time and memory usage are tested solving the Stokes flow with the analytical solution proposed by Donea and Huerta (2003) (Section 10.2).

The thermo-mechanics of crust-mantle systems is described by means of the conservation of mass, momentum and energy equations, expressed as follows:

$$\frac{\partial \rho}{\partial t} + \nabla \cdot (\rho \mathbf{u}) = 0 \quad (1)$$

$$-\nabla p + \nabla \cdot \boldsymbol{\tau} + \rho \mathbf{g} = 0 \quad (2)$$

$$\rho C_p \left(\frac{\partial T}{\partial t} + \mathbf{u} \cdot \nabla T \right) = \nabla \cdot (k \nabla T) + H_{tot} \quad (3)$$

where ρ is the density, \mathbf{u} is the velocity, p is the pressure, $\boldsymbol{\tau}$ is the deviatoric stress, \mathbf{g} is the gravity acceleration, C_p is the specific heat at constant pressure, T is the temperature, k is the thermal conductivity and H_{tot} is the total internal heat production. Density variations due to temperature are generally small enough to assume the density as constant ($\rho = \rho_0$) in Eq. 1 and in Eq. 3, while it must be treated as a variable in the buoyancy term of Eq. 2, such

¹<http://mumps.enseeih.fr/>

that

$$\rho = \rho_0(1 - \alpha(T - T_0))$$

where ρ_0 is the density at a reference temperature T_0 and α is the coefficient of thermal expansion. Eq. 1 then can be rewritten as

$$\nabla \cdot \mathbf{u} = 0 \quad (4)$$

This simplification is known as the extended Boussinesq approximation.

The time step dt is chosen in according to Courant-Friedrichs-Lowy condition (Anderson, 1995), such that

$$dt = C_n \min \left(\frac{\Delta x}{\max |\mathbf{u}|}, \frac{(\Delta x)^2}{\kappa} \right)$$

where $0 < C_n < 1$ is the Courant (CFL) number, Δx is the minimum dimension of smallest element, $\max |\mathbf{u}|$ is the maximum velocity calculated on the entire domain and $\kappa = \frac{k}{\rho C_p}$ is the thermal diffusivity (Thieulot, 2014).

2 Lagrangian markers

Elemental properties (density, viscosity, thermal conductivity, specific heat and thermal expansion) needed to solve Eqs. 4, 2 and 3 are related to the composition of each element, determined by means of Lagrangian markers that are characteristic of different materials in the domain. Elemental properties (with the sole exception of the viscosity) are calculated using an arithmetic mean, as

$$P_e = \frac{1}{n} \sum_{i=1}^n P_i$$

where P_e is the elemental property, P_i is the property characteristic of the material of each marker and n is the number of markers of the element. Differently, the average scheme for the elemental viscosity can be chosen between harmonic, geometric and arithmetic mean. Markers can be placed regularly or randomly at the beginning of the simulation and their advection is performed by either a 2nd-order or a 4th-order Runge-Kutta in space, interpolating the velocity field on each marker by means of the shape functions (see Section 10.3). The interpolated velocity is then corrected by means of the Conservative Velocity Interpolation (CVI), which introduces a corrective term to reduce dispersion and clustering of particles in both steady state and time-dependent (Wang et al., 2015) (see Section 10.4).

The initial distribution of the markers is created using the open-source code library Geodynamic World Builder (Fraters et al., 2019). During the simulation, each marker carries memory of temperature, pressure and accumulated strain, which are determined interpolating the relative nodal parameter. In particular, pressure is interpolated onto each marker after the smoothing procedure. The number of markers contained in each element is maintained between n_{min} and n_{max} . When in an element there are less markers than n_{min} the code adds random markers to reach the n_{min} , while if the number is higher than n_{max} some of them are randomly deleted. When new markers are added, they assume the properties of the nearest marker. In this way elements are never empty and maintain a number of markers inside a prefixed range.

3 The momentum equation

The penalty method is implemented so that Eq. 4 can be written as:

$$\nabla \cdot \mathbf{u} + \frac{p}{\lambda} = 0 \quad (5)$$

where λ is the so-called penalty parameter, which should be 6-7 orders of magnitude larger than the shear viscosity to ensure that mass conservation is satisfied (Donea and Huerta, 2003; Thieulot, 2014).

The deviatoric stress tensor in Eq. 2 can be written in terms of the strain rate tensor as $\boldsymbol{\tau} = 2\eta\dot{\epsilon}$, with $\dot{\epsilon} = \frac{1}{2}(\nabla\mathbf{v} + (\nabla\mathbf{v})^T)$. Therefore, Eq. 2 can be rewritten as:

$$-\nabla p + \nabla \cdot (\eta(\nabla\mathbf{v} + (\nabla\mathbf{v})^T)) + \rho\mathbf{g} = 0 \quad (6)$$

Finally, using pressure from Eq. 5, Eq. 6 can be rewritten as:

$$\lambda\nabla(\nabla \cdot \mathbf{v}) + \nabla \cdot (\eta(\nabla\mathbf{v} + (\nabla\mathbf{v})^T)) + \rho\mathbf{g} = 0 \quad (7)$$

The penalty method is been associated to the iterative Uzawa method, as described in detail in Dabrowski et al. (2008) and Thieulot (2014) (see Section 10.5). Results of benchmarks performed to verify the correctness in the implementation of Eq. 7 are shown in Sections 10.6 and 10.7.

To support large viscosities variations the penalty parameter is related to the effective elemental viscosity by means of a dimensionless coefficient, so that $\lambda = \lambda_e(e)\eta_{eff}(e)$ (Marotta et al., 2006; Dabrowski et al., 2008; Thieulot, 2014). Benchmark of the falling block (Gerya and Yuen, 2003; Gerya, 2010; Thieulot, 2011) is performed to verify that the code can correctly deal buoyancy driven flows with strong viscosity contrasts (Section 10.8).

4 Sticky air and free surface

The Earth's surface can be treated by means of either the so-called sticky-air or a true free surface method, both of them implemented in the code. In the sticky-air method the surface is approximated with the introduction of a buoyant layer with a viscosity at least four orders of magnitude lower than the crust (Schmeling et al., 2008; Crameri et al., 2012) and the interface between lithosphere and air is defined using a chain of passive markers that are advected as the Lagrangian markers. The correctness of the evolution of the markers chain is tested with the experiment of a 2D time-dependent Stokes sphere below a free surface and compared with results from ASPECT² (Kronbichler et al., 2012; Heister et al., 2017; Bangerth et al., 2020a,b) (Section 10.9). In the true free surface case the top boundary is assumed stress-free and velocities are not fixed. In this case topography variations are described by vertical deformations of the mesh that depend on the velocity field of the nodes that identify the free surface, while horizontal deformations are not taken into account. This procedure is known as the Arbitrary Lagrangian-Eulerian (ALE) method and its implementation follows the technique described in Thieulot (2011). However, although the implementation of a true free surface better reproduces laboratory experiment, extremely small time steps can be necessary to maintain stability (Kaus et al., 2010; Quinquis et al., 2011; Thieulot, 2014). Therefore, the stability algorithm proposed by Kaus et al. (2010) is implemented to avoid instabilities due to high density differences at the free surface when using too large time steps. The implementation of this algorithm are tested by performing the experiment described by Kaus et al. (2010) (Section 10.10).

The topography relaxation benchmark proposed by Crameri et al. (2012) is performed to verify that the code correctly recovers topography variations in case of both the sticky-air and the true free surface method (Section 10.11). Finally, Section 10.12 show the results of the spontaneous subduction experiment described by Schmeling et al. (2008).

5 Erosion and sedimentation

Surface processes at the lithosphere-air interface are implemented taking into account fluvial erosion (long-range processes), hillslope processes (short-range processes) and failure of slopes exceeding a threshold angle θ (Burov and Cloetingh, 1997; Whipple and Tucker, 1999; Sacek et al., 2012; Croissant and Braun, 2014; Ueda et al., 2015; Beucher and Huismans, 2020). Erosion rates \dot{E}_{lr} due to long-range processes can be described by a stream power law equation (Whipple and Tucker, 1999; Ueda et al., 2015; Beucher and Huismans, 2020), in according to

$$\dot{E}_{lr} = K_f A^{m_e} \nabla h^{n_e} \quad (8)$$

where K_f is the erodibility coefficient, A is the upstream drainage area, ∇h is the slope and m_e and n_e are parameters chosen in to constrain the ratio m_e/n_e between 0.35 and 0.8 (Croissant and Braun, 2014; Ueda et al., 2015; Beucher and Huismans, 2020). Erosion rates \dot{E}_{sr} due to short-range processes are implemented by assuming that transport is linearly proportional to slope (Burov and Cloetingh, 1997; Ueda et al., 2015; Beucher and Huismans, 2020), in according to

$$\dot{E}_{sr} = K_d \nabla^2 h \quad (9)$$

where K_d is the effective diffusivity. In addition, the slope is modified if it still exceeds a threshold angle after long- and short-range processes (Ueda et al., 2015).

Offshore sedimentation processes are implemented similarly to hillslope processes but with a depth-dependent coefficient (Sacek et al., 2012; Beucher and Huismans, 2020). The sedimentation rate \dot{S} is calculated as

$$\dot{S} = K_s \nabla^2 h \quad (10)$$

with

$$K_s = K_s^* \exp\left(\frac{h - h_{sl}}{h_0}\right) \quad (11)$$

where K_s^* is a constant, h_{sl} is the sea level and h_0 is a characteristic length. In case of sticky air, slope is determined by means of the markers chain, which is vertically corrected considering erosion and sedimentation rates. After the correction, continental markers above the markers chain are transformed in air markers and air markers below the markers chain become sediments. Similarly, slope is determined considering the nodes on the top boundary in case of true free surface and they are vertically corrected as for the markers chain. In this case, continental markers above the top boundary are simply deleted.

²<https://aspect.geodynamics.org/>

6 Non-linear rheologies

Non-linear rheologies are implemented combining viscous creep (dislocation and diffusion) and plastic yielding. For each marker, diffusion and dislocation viscosity ($\eta_{df|ds}$) can be determined as follows (Karato and Wu, 1993; Wang et al., 2016):

$$\eta_{df|ds} = \left(\frac{d^m}{A} \right)^{\frac{1}{n}} I_2^{\frac{(1-n)}{n}} \exp \left(\frac{Q + pV}{nRT} \right) \quad (12)$$

where d is the grain size, m is the grain size exponent, n is the stress exponent, A is the pre-exponential factor, I_2 is the square root of the second invariant of the strain rate tensor, Q is the activation energy, p is the pressure, V is the activation volume, R is the gas constant and T is the temperature. Pressures and temperatures are determined by the interpolation of the nodal parameters, while strain rates are calculated by means of the derivative of the velocities on the nodes. In case of diffusion creep $n = 1$ and $m > 0$, in case of dislocation creep $n > 1$ and $m = 0$. The viscous creep η_{cp} is then calculated as the harmonic average between η_{df} and η_{ds} :

$$\eta_{cp} = \left(\frac{1}{\eta_{df}} + \frac{1}{\eta_{ds}} \right)^{-1} \quad (13)$$

The implementation of the non-linear viscous creep viscosity depending on the strain rate is tested by means of the slab detachment benchmark (Section 10.13).

Plastic yielding is implemented rescaling η_{cp} in order to limit the stress below the yield stress σ_y (Thieulot et al., 2008; Thieulot, 2014; Glerum et al., 2018), obtaining

$$\eta_{pl} = \frac{\sigma_y}{2I_2} \quad (14)$$

where η_{pl} is the plastic viscosity and the yield stress is determined following the Drucker-Prager criterion, such as

$$\sigma_y = C \cos(\phi) + p \sin(\phi) \quad (15)$$

where C is the cohesion and ϕ is the internal friction angle. In case of negative pressure it is imposed equal to 0, so that negative yield stress are excluded. The correctness of the non-linear solution in case of plastic viscosity with variable internal friction angle is verified performing indenter and brick experiments (Sections 10.14 and 10.15, respectively).

Strain softening is taken into account for both viscous creep and plastic viscosity (Huismans and Beaumont, 2003; Babeyko and Sobolev, 2005; Huismans et al., 2005; Sobolev and Babeyko, 2005; Warren et al., 2008) by means of the accumulated strain ϵ memorised by each marker. Softening in the viscous creep determines a linear decrease of η_{vc} by means of a viscous strain softening factor W_S that increases linearly from W_{S_0} to W_{S_∞} for $\epsilon_{S_0} < \epsilon_S < \epsilon_{S_\infty}$ (Warren et al., 2008). This viscous softening can be related to strain-induced grain size reduction (Warren et al., 2008). Differently, plastic softening is simulated with a linear decrease of internal friction angle $\phi(\epsilon)$ and cohesion $C(\epsilon)$ in according to

$$\phi(\epsilon) = \phi_0 + (\phi_\infty - \phi_0) \frac{\epsilon - \epsilon_0}{\epsilon_\infty - \epsilon_0} \quad (16)$$

$$C(\epsilon) = C_0 + (C_\infty - C_0) \frac{\epsilon - \epsilon_0}{\epsilon_\infty - \epsilon_0} \quad (17)$$

where ϕ_0 , C_0 and ϕ_∞ , C_∞ are internal friction angle and cohesion for ϵ_0 and ϵ_∞ , respectively (Huismans and Beaumont, 2003; Huismans et al., 2005; Warren et al., 2008; Thieulot, 2014). Plastic softening approximates deformation-induced softening of faults and brittle shear zones (Warren et al., 2008).

Plastic yielding and viscous creep are then combined to obtain a viscoplastic viscosity η_{vp} as follows, assuming that they are independent processes (Karato, 2008; Glerum et al., 2018):

$$\eta_{vp} = \min(\eta_{cp}, \eta_{pl}) \quad (18)$$

Finally, effective viscosity η_{eff} is capped by the minimum and the maximum viscosity (η_{min} and η_{max} , respectively) to avoid extremely low or high viscosity (Glerum et al., 2018) as follows

$$\eta_{eff} = \min(\max(\eta_{vp}, \eta_{min}), \eta_{max}) \quad (19)$$

Viscous creep and plastic yielding are non-linear rheologies because of their dependence on the velocity field through pressure and strain rates. Therefore, the solution is determined by means of Picard-type iterations, until convergence of the velocity field (Glerum et al., 2018). The convergence is verified at each iteration i via the nonlinear residual \mathcal{R}^i that can be determined as

$$\mathcal{R}^i = \mathbb{K}(\eta_{eff}(\boldsymbol{\epsilon}^{i-1}, p^{i-1})) \cdot \boldsymbol{v}^{i-1} - \boldsymbol{f}^i \quad (20)$$

where \mathbb{K} is the Stiffness matrix and \mathbf{f} is the right hand side vector (Spiegelman et al., 2016; Glerum et al., 2018). The L_2 -norm is extracted from \mathcal{R}^i and it is normalised as follows

$$\frac{\|\mathcal{R}^i\|_2}{\|\mathcal{R}^0\|_2} \quad (21)$$

where $\|\mathcal{R}^0\|_2$ is the L_2 -norm of the first nonlinear iteration. Since often the normalised nonlinear residual drop very quickly over the first 2-3 iterations, also the L_2 -norm of velocity and pressure residuals are calculated as

$$\frac{\|\Delta \mathbf{v}\|_2}{\|\mathbf{v}\|_2} = \frac{\|\mathbf{v}_i - \mathbf{v}_{i-1}\|_2}{\|\mathbf{v}_i\|_2} \quad (22)$$

and

$$\frac{\|\Delta p\|_2}{\|p\|_2} = \frac{\|p_i - p_{i-1}\|_2}{\|p_i\|_2} \quad (23)$$

respectively. Iterations are performed until either maximal number of non-linear iterations (it_{max}) is reached or all the normalised nonlinear residual, the velocity residual and the pressure residual converge under a defined tolerance tol .

7 The energy equation

The stabilisation of the advection term of the energy equation (Eq. 3) needed to avoid possible oscillations in the thermal solution in the case when advection dominates over diffusion, is implemented by means of a streamline-upwind Petrov–Galerkin (SUPG) method, for which the advection term is modified follows the discussion in Thieulot (2011) and Thieulot (2014) (see Section 10.16 for benchmark). The total internal heat production H_{tot} in Eq. 3 includes radiogenic heating H_r , shear heating H_s and adiabatic heating H_a , where

$$H_s = 2\eta\dot{\epsilon} : \dot{\epsilon} = 2\eta(\dot{\epsilon}_{xx}^2 + \dot{\epsilon}_{yy}^2 + 2\dot{\epsilon}_{xy}^2) \quad (24)$$

and

$$H_a = T\alpha \frac{Dp}{Dt} \approx -\alpha T \rho g_y v \quad (25)$$

The correctness of the implementation and the computation of shear and adiabatic heating is verified performing an exercise with an analytical solution (Section 10.17) and Exercise 9.4 in Gerya (2010) (Section 10.18). Furthermore, mantle convection and thin layer entrainment benchmarks (Sections 10.19 and 10.21, respectively) are performed to verify that the code solve correctly Eqs. 7 and 3 in case of a temperature field characterised by an initial perturbation and with a temperature-dependent density. At last, the viscoplastic mantle convection benchmark is performed to check also the viscoplasticity in case of a initial perturbed temperature field (Section 10.20).

8 Phase transitions and hydration

Variations of effective density, specific heat and coefficient of thermal expansion during the evolution of crustal and mantle materials at different pressure-temperature (p - T) conditions are computed by means of version 6.8.6 of Perple.X software package (Connolly, 2005), similarly to the implementation described in Marotta et al. (2020). By default, mineral assemblages and properties of each lithology (oceanic crust, lower and upper continental crust, sediments and dry or hydrated mantle) are calculated for temperatures from 330 K to 1600 K, with increments of approximately 4 K, and pressures from 0.1 GPa to 30 GPa, with increments of approximately 0.03 GPa, for a total of almost 100000 points.

The introduction of phase transitions produces two main effects that must be taken into account in numerical models: variations in density and release/absorption of latent heat (Ismail-Zadeh and Tackley, 2010). Effects of density variations on buoyancy force in the momentum equation (Eq. 7) are taken into account considering effective coefficient of thermal expansion (Christensen and Yuen, 1985; Zhong et al., 2015). Similarly, effects of latent heat in the energy equation (eq 3) are taken into account by considering effective specific heat and coefficient of thermal expansion (Christensen and Yuen, 1985; Ismail-Zadeh and Tackley, 2010; Zhong et al., 2015). Effective density, specific heat and coefficient of thermal expansion are included in Perple.X files and are assumed by each Lagrangian marker in according to its p - T conditions.

Hydration processes related to dehydration of subducting lithosphere (Schmidt and Poli, 1998; Liu et al., 2007; Faccenda et al., 2009; Faccenda and Mancktelow, 2010; Faccenda, 2014; Rosas et al., 2016) strongly influence the thermo-mechanics inside the mantle wedge, mainly because of both weakening effects on the mantle rheology and density variations in case of mantle serpentinization (Gerya and Stockhert, 2002; Honda and Saito, 2003; Arcay et al., 2005; Roda et al., 2010; Regorda et al., 2017). In the case that hydration is switched on, the amount of bound and free water is memorised by each marker, following the implementation of Quinquis and Buiter (2014); hydration and

dehydration processes are related to the amount of bound water of each marker and to the maximum amount of water it can transport, i.e. if the amount of bound water exceeds the maximum amount of water, the marker dehydrates and releases free water that can hydrate under-saturated markers. Maximum water content of each marker is determined as function of lithology and p - T conditions and it is calculated using Perple_X, in the same way than effective density, specific heat and coefficient of thermal expansion. Bound water is advected together with the markers, neglecting the effect of bound water diffusion, while free water simply migrates vertically and is not coupled to the solid-phase flow of the mantle wedge (Arcay et al., 2005; Quinquis and Buiter, 2014). The correctness of the migration scheme of the free water and its absorption into bound water by under-saturated markers are verified performing the experiment described in Quinquis and Buiter (2014) (Sec. 10.22).

The mantle viscosity weakening related to the amount of water has been extensively studied (Chopra and Peterson, 1981; Hirth and Kohlstedt, 2003) and it is implemented in according to Arcay et al. (2005) and Horiuchi and Iwamori (2016), as follows

$$\eta_{wet} = \eta_{dry} \left(\left[1 - \frac{1}{f_v} \right] \exp \left(-\frac{[OH^-]}{[OH^-]_0} \right) + \frac{1}{f_v} \right) \quad (26)$$

where f_v is the viscosity reduction factor between dry and wet conditions, $[OH^-]$ is the water content and $[OH^-]_0$ is a reference water content set to 620 ppm (0.062 wt.%) (Arcay et al., 2005). By default, f_v is set to 100, in according to Arcay et al. (2005) and Horiuchi and Iwamori (2016).

9 Mantle melting

Melt fraction in the mantle depends on temperature (T , in °C), pressure (p , in GPa) and the water content in the melt (X_{H_2O} , in wt.%). The determination of the melt fraction M is implemented as explained by Katz et al. (2003), according to the successive modification by Langmuir et al. (2006) and Kelley et al. (2010), as follows

$$M(p, T, X_{H_2O}) = -T + T_{sol} + (x_t \cdot \ln(p + y_t)) \cdot X_{H_2O} - + K_m \left(\frac{X_{H_2O}^{bulk}}{D_{H_2O}(1 - X_{H_2O}) + X_{H_2O}} \right)^\gamma \quad (27)$$

where T_{sol} is the temperature of the dry solidus, D_{H_2O} is the partition coefficient and $x_t \cdot \log(p + y_t)$ indicates the pressure dependence of the melting curve (Kelley et al., 2010). x_t , y_t , K_m and γ are parameters chosen in according to Kelley et al. (2010). However, X_{H_2O} depends on the melt fraction as

$$X_{H_2O}(M) = \frac{X_{H_2O}^{bulk}}{D_{H_2O} + M(1 - D_{H_2O})} \quad (28)$$

and a numerical solution can be found using a root-finder method (Katz et al., 2003; Wang et al., 2016). Furthermore, the content of water in the melt is limited by the pressure-dependent saturation concentration of water in the melt, determined as

$$X_{H_2O}^{sat} = \chi_1 p^{\lambda_m} + \chi_2 p \quad (29)$$

where χ_1 , χ_2 and λ_m are parameters chosen according to Katz et al. (2003), Langmuir et al. (2006) and Kelley et al. (2010). The correctness in the determination of melt fractions and water contents in the melt are tested comparing model results with experimental curves obtained by Katz et al. (2003) (Sec. 10.23).

In case of melting, viscous creep viscosity (η_{vp}) is modified according to Wang et al. (2016), as

$$\eta_{melt} = \eta_{vp} \cdot \exp(\alpha_m M) \quad (30)$$

where α_m are melt fraction factors for dislocation and diffusion creep, chosen in according to Wang et al. (2016).

Effective density (ρ_{eff}) for partially molten rocks is calculated as

$$\rho_{eff} = \rho_s(1 - M) + \rho_m M \quad (31)$$

where ρ_s and ρ_m are the densities of the solid and the molten rock, respectively (Gerya and Yuen, 2003; Wang et al., 2016). The density of the solid rock is extracted by Perple_X, while the density of the molten portion is calculated as

$$\rho_m(p, T) = \rho_0 [1 - \alpha(T - T_0)] [1 + \beta(p - p_0)] \quad (32)$$

where ρ_0 is the density at the reference temperature (T_0) and pressure(p_0), and α and β are the thermal expansion and compressibility coefficients, respectively (Gerya and Yuen, 2003; Wang et al., 2016).

As for the phase transitions, effects of density variations on buoyancy force in the momentum equation (Eq. 7) are taken into account considering effective coefficient of thermal expansion. Similarly, latent heat due to melting/crystallisation can be implicitly included in the energy equation (Eq. 3) by considering effective specific heat ($C_{p_{eff}}$) and thermal expansion (α_{eff}) of the partially molten rocks, in according to

$$C_{p_{eff}} = C_p + H_L \left(\frac{\partial M}{\partial T} \right)_p \quad (33)$$

$$\alpha_{eff} = \alpha + \rho \frac{H_L}{T} \left(\frac{\partial M}{\partial p} \right)_T \quad (34)$$

where C_p and α are the specific heat and the coefficient of thermal expansion of the solid rock, respectively, and H_L is the latent heat of the molten rock (Gerya and Yuen, 2003, 2007; Ismail-Zadeh and Tackley, 2010).

10 Benchmarks

10.1 Error measurements

In order to determine the accuracy of velocity and pressure field of the benchmarks, the L_2 -norm is computed by numerical integration on the Gauss-Legendre quadrature points. L_2 -norm for pressure and velocity errors can be evaluated as

$$\begin{aligned} \text{err}_p &= \sqrt{\sum_{i=1}^{n_e} \sum_{q=1}^{n_q} (|p_i^n(r_q) - p_i^a(r_q)|^2) w_q |J_q|} \\ \text{err}_v &= \sqrt{\sum_{i=1}^{n_e} \sum_{q=1}^{n_q} (|u_i^n(r_q) - u_i^a(r_q)|^2 + |v_i^n(r_q) - v_i^a(r_q)|^2) w_q |J_q|} \end{aligned}$$

respectively, where n_e is the number of elements, n_q is the number of quadrature points per element, $p_i^n(r_q)$ and $p_i^a(r_q)$ are the numerical and analytical pressure, respectively, in each quadrature point q , w_q and J_q are the weight and the Jacobian at the quadrature point q , $u_i^n(r_q)$, $v_i^n(r_q)$, $u_i^a(r_q)$ and $v_i^a(r_q)$ are the numerical and analytical velocities, respectively, in each quadrature point q .

Other quantities used as comparison with original benchmarks are the root-mean-square velocity over the whole domain and over the surface

$$\begin{aligned} v_{\text{rms}} &= \sqrt{\int_{\Omega} |\mathbf{v}|^2 d\Omega} \\ v_{\text{rms}}^{top} &= \sqrt{\int_0^1 u^2 \Big|_{y=1} dx} \end{aligned}$$

respectively, top and bottom Nusselt numbers

$$\text{Nu}^{top/bottom} = - \int_0^1 \frac{\partial T}{\partial y} \Big|_{y=1/y=0} dx$$

the average rate of work done against gravity

$$\langle W \rangle = \int_{\Omega} T u_y d\Omega$$

the average rate of viscous dissipation

$$\langle \Phi \rangle = \int_{\Omega} \tau_{ij} \dot{\epsilon}_{ij} d\Omega$$

and the percentage error between $\langle W \rangle$ and $\langle \Phi \rangle / Ra$

$$\delta = \frac{\left| \langle W \rangle - \frac{\langle \Phi \rangle}{Ra} \right|}{\max \left(\langle W \rangle, \frac{\langle \Phi \rangle}{Ra} \right)} \times 100$$

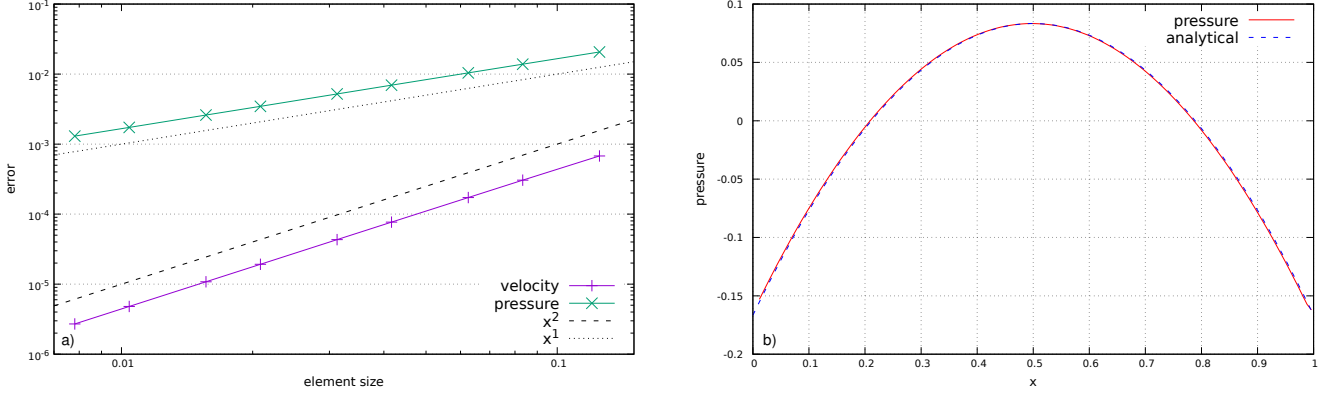


Figure 1: Velocity and pressure error for the Stokes flow experiment between generated and analytical solution as a function of element size (panel a), and comparison between smoothed pressure and analytical solution as function of x coordinate for a grid resolution of 128×128 elements (panel b).

10.2 Stokes flow

The problem consists of determining velocity field (u, v) and pressure p in case of a manufactured solution with prescribed body forces such as

$$\begin{aligned} b_1 &= (12 - 24y)x^4 + (-24 + 48y)x^3 + (-48y + 72y^2 - 48y^3 + 12)x^2 + \\ &\quad + (-2 + 24y - 72y^2 + 48y^3)x + 1 - 4y + 12y^2 - 8y^3 \\ b_2 &= (8 - 48y + 48y^2)x^3 + (-12 + 72y - 72y^2)x^2 + (4 - 24y + 48y^2 - 48y^3 + \\ &\quad + 24y^4)x - 12y^2 + 24y^3 - 12y^4 \end{aligned}$$

for which the exact solution is:

$$\begin{aligned} u(x, y) &= x^2(1-x)^2(2y-6y^2+4y^3) \\ v(x, y) &= -y^2(1-y)^2(2x-6x^2+4x^3) \\ p(x, y) &= x(1-x) - \frac{1}{6} \end{aligned}$$

The domain is a unit square a constant viscosity ($\eta = 1$) and the penalty parameter is set to $\lambda = 10^7$. Velocity boundary conditions are set to no slip ($\mathbf{v} = \mathbf{0}$) on all boundaries. The problem is performed for different grid resolution between 8×8 and 1024×1024 elements.

The errors between the analytical solution and the numerical prediction of the velocity and the pressure field are calculated as in Section 10.1. Fig. 1a shows that both velocity and pressure field converge to the exact solution with the decrease of the element size, following the theoretical convergence rate. The convergence of pressure, in contrast with the observation by Donea and Huerta (2003) for $Q_1 \times P_0$ elements, indicate the effectiveness of the smoothing procedure. Smoothed pressure field for grid resolution of 128×128 elements is shown in Fig. 1b (continuous red line), in comparison with the analytical solution (dashed blue line). Solve times and memory usage needed to generate the solution are shown in Fig. 2. All data can be found at https://github.com/aleregora/Benchmarks/tree/main/Solver/Stokes_Flow.

10.3 Markers advection

The 2nd-order Runge-Kutta advection scheme in space is tested by means of the Zalesak disk test (Zalesak, 1979; Thieulot, 2014). The benchmark is performed in a unit square domain with a grid resolution of 32×32 elements and 1000000 markers and values of Courant number between 0.25 and 1. At $t = 0$, the disk is centred at position $(0.5; 0.75)$ with a radius $R = 0.15$ and has a vertical fissure 0.05 wide and 0.2 high (orange in Fig. 3) and with the velocity field prescribed in the entire domain as

$$\begin{aligned} u(x, y) &= 2\pi \left(y - \frac{L_x}{2} \right) \\ v(x, y) &= -2\pi \left(x - \frac{L_x}{2} \right) \end{aligned}$$

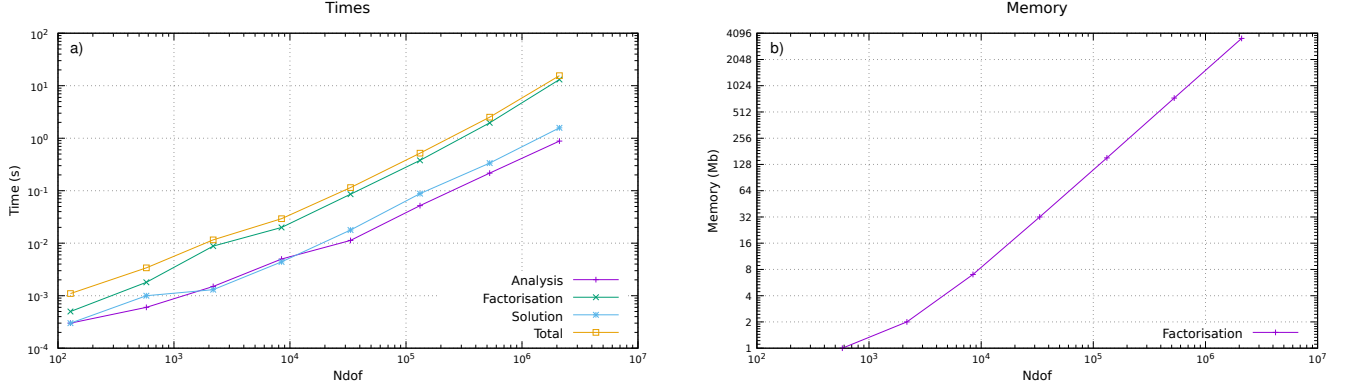


Figure 2: Panel a) Analysis, factorisation, solution and total solve times (panel a) and factorisation memory usage (panel b) as a function of the total number of degrees of freedom for the Stokes flow experiment.

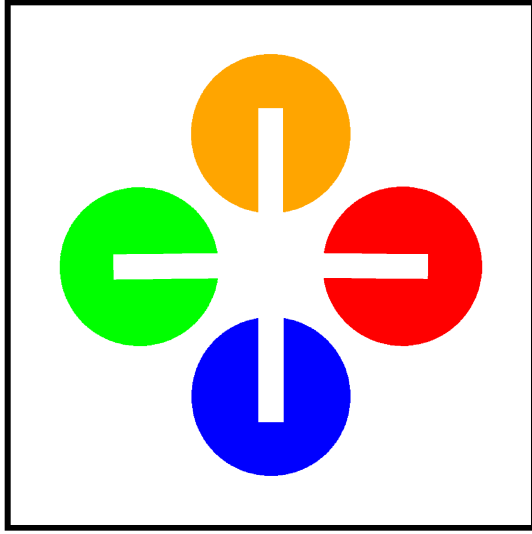


Figure 3: Position of the Zalesak disk at $t = 0, 0.25, 0.5$ and 0.75 (orange, red, blue and green, respectively) for the case with Courant number of 1.

the markers are back to their initial location after a 2π rotation ($t = 1$). The clockwise rotation of the disk at $t = 0.25, 0.5$ and 0.75 is shown in Fig. 3 (red, blue and green, respectively). The distance from the centre of 1 marker is calculated throughout the rotation to evaluate the error for different values of Courant number. As expected, the error increase with the increasing of the time step, as shown in Fig. 4. All data can be found at https://github.com/aleregorde/Benchmarks/tree/main/Advection/Zalesak_Disk.

10.4 Conservative Velocity Interpolation (CVI)

The CVI correction is checked by means of the Stokes flow experiment by [Donea and Huerta \(2003\)](#), as presented in [10.2](#). The advection of Lagrangian markers is performed using either a 2nd-order or a 4th-order Runge-Kutta scheme with $CFL=0.5$ and an initial random distribution of 25 markers per element. Fig. 5 shows the minimum and maximum values of markers per element throughout the experiment with and without the CVI correction and using different Runge-Kutta schemes. The introduction of the CVI correction allows the tests to run for times longer than $t = 2000$ without show empty elements, while tests without the CVI correction stop at approximately $t = 600$, when at least one element goes empty. Fig. 6 shows the different number of markers per element and the markers distribution at $t = 600$ obtained without and with the CVI correction (panels b and c, respectively) in case of a 2nd-order Runge-Kutta scheme. All data can be found at <https://github.com/aleregorde/Benchmarks/tree/main/Advection/CVI>.

10.5 Poiseuille flow

The domain is a rectangle with $L_x = 2$ and $L_y = 1$ and constant density and viscosity ($\rho = 1$ and $\eta = 1$), gravity acceleration $\mathbf{g} = \mathbf{0}$ and penalty parameter $\lambda = 10^8$. The grid is composed by 40×20 elements. Velocity boundary



Figure 4: Distance from the centre as function of time for values of Courant number of 0.25, 0.3, 0.5, 0.75 and 1 (green, orange, blue, black and red, respectively). R indicates the distance from the centre considering a perfect circle trajectory.



Figure 5: Maximum and minimum number of markers per element throughout the experiment, with (green and orange lines) or without (purple and blue lines) the CVI correction and using either a 2nd-order (blue and orange lines) or a 4th-order (purple and green lines) Runge-Kutta scheme.

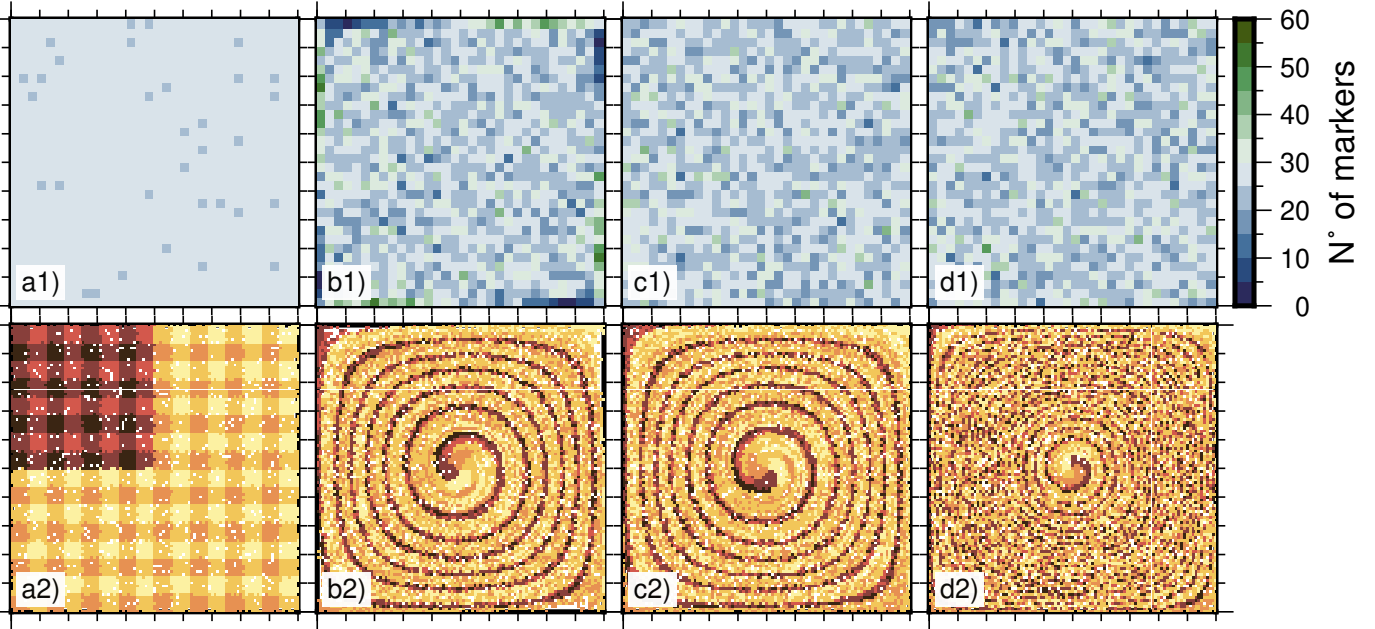


Figure 6: Number of markers per element and markers distribution through time using 2nd.order Runge-Kutta scheme. Panels a: number of markers per element (panel a1) and distribution of the markers (panel a2) after the first iteration; panels b and c: comparison between number of markers per element (panels b1 and c1) and markers distribution (panels b2 and c2) without and with the CVI correction at $t = 600$; panels d: number of markers per element (panel d1) and markers distribution (panel d2) in case of CVI correction at $t = 2000$.

conditions are set to no slip ($\mathbf{v} = \mathbf{0}$) at the top and the bottom, and a parabolic profile is imposed on the sides, with $u = y(1 - y)$ and $v = 0$. The analytical solution is then given by:

$$\begin{aligned} u(x, y) &= y(1 - y) \\ v(x, y) &= 0 \\ p(x, y) &= 2\eta \left(\frac{L_x}{2} - x \right) \end{aligned}$$

The velocity field predicted by the model follows the expected parabolic profile (Fig. 7a and Fig. 8a) and, in case of the classic penalty method with no iterations, the pressure is clearly related to the divergence by means of the penalty parameter (Fig. 7b and c and Fig. 8b). Fig. 7d shows that one Uzawa iteration is sufficient to bring the divergence down to 10^{-15} , with no correlation with the pressure field. All data can be found at https://github.com/aleregora/Benchmarks/tree/main/Momentum_equation/Poiseuille%20Flow.

10.6 Instantaneous 2D sphere

The domain is a unit square with gravity $\mathbf{g} = (0, -1)$. The fluid has constant density and viscosity ($\rho_f = 1$ and $\eta_f = 1$). The sphere is in the middle of the domain with a radius $R = 0.123456798$ and has constant density and viscosity ($\rho_s = 10^{-2} + \rho_f$ and $\eta_s = 10^3 \cdot \eta_f$). We distinguish three different types of velocity boundary conditions:

1. FS: free slip conditions on all sides.
2. NS: no slip conditions on all sides.
3. OT: free slip conditions on the sides and the bottom, and open boundary at the top.

All three cases are performed for different grid resolutions, between 16×16 and 512×512 elements with 50 randomly distributed markers per element, and different average schemes for the viscosity (harmonic, geometric and arithmetic). The velocity in the centre of the sphere $\mathbf{v}(0.5; 0.5)$, minimum and maximum velocities ($u_{min}, u_{max}, v_{min}, v_{max}$) and pressures (p_{min}, p_{max}) on the entire domain, v_{rms} and average pressure on the entire domain (p_{avg}) are compared with solutions generated by ASPECT (Kronbichler et al., 2012; Heister et al., 2017; Bangerth et al., 2020a,b) and all results can be found at https://github.com/cedrict/fieldstone/tree/master/images/stokes_sphere2D and https://github.com/aleregora/Benchmarks/tree/main/Momentum_equation/Instantaneous_2D_Sphere. Results in terms of the v_{rms} for NS model are also shown in Fig. 9.

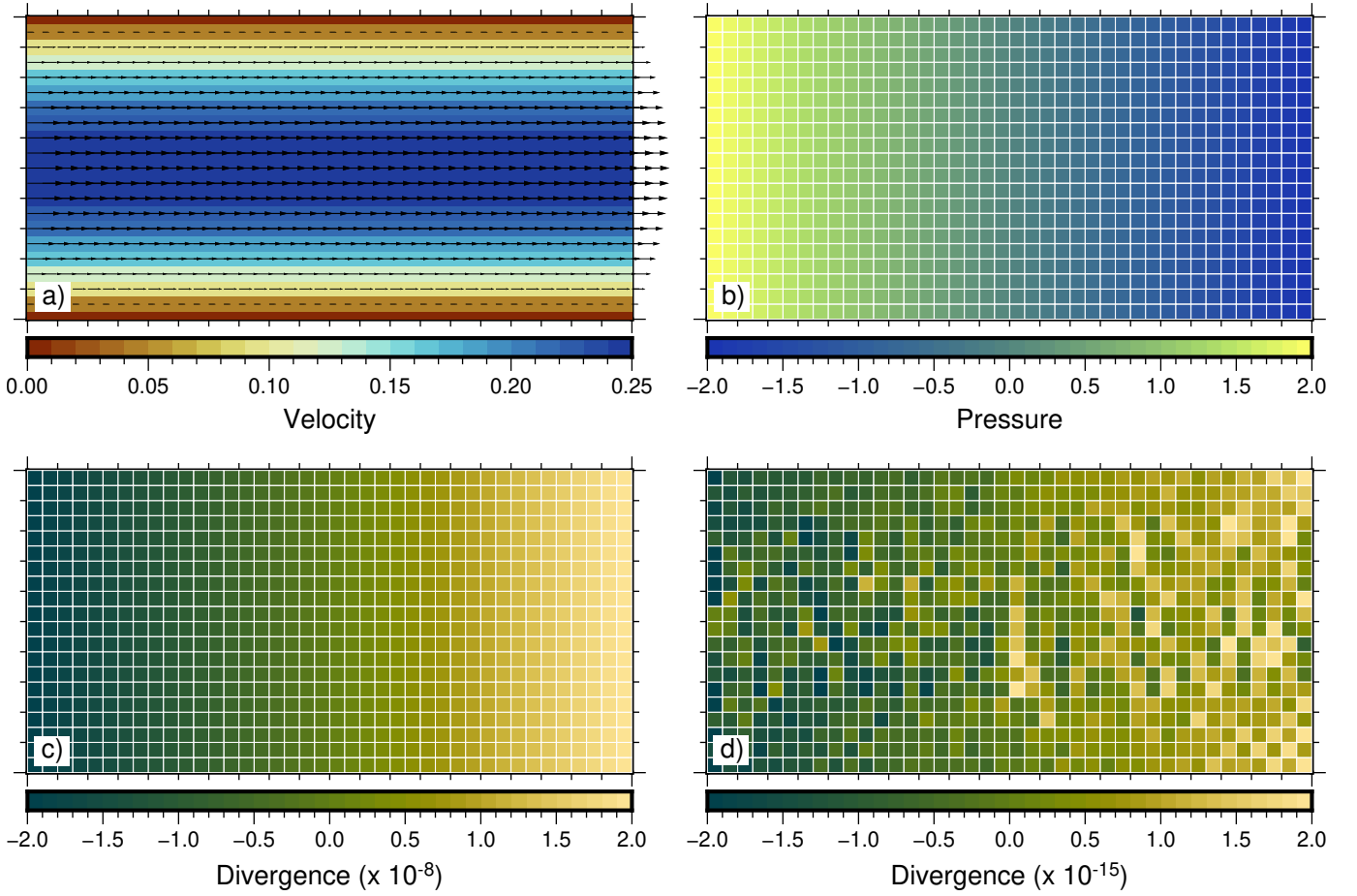


Figure 7: Velocity field (panel a), pressure (panel b) and divergence velocity of a Poiseuille flow in case of the classic penalty method (no iterations) and after one Uzawa iteration (panel c and d, respectively).

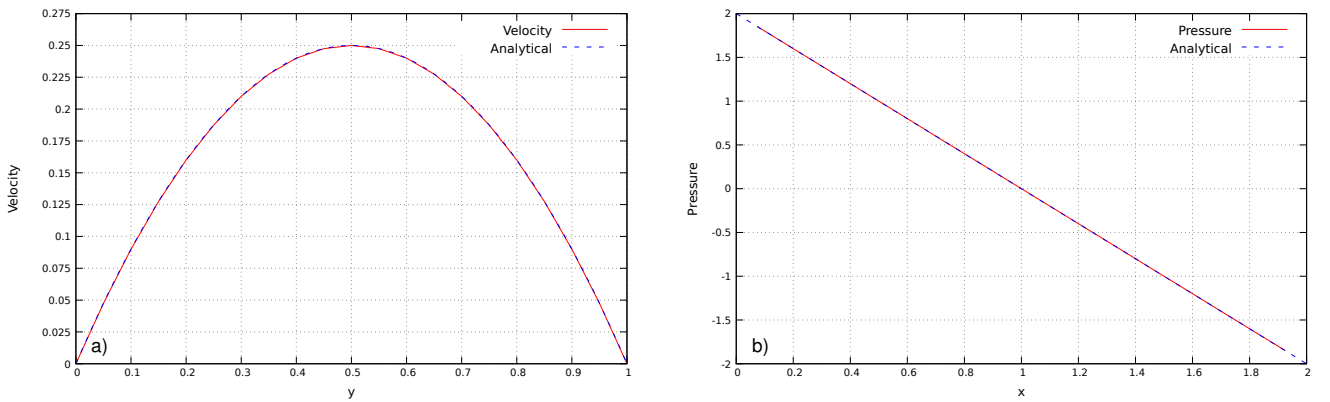


Figure 8: Velocity (panel a) and pressure (panel b) field predicted by the model for a Poiseuille flow with respect with their analytical solutions. The velocity field is plotted as function of the vertical coordinate in $L_x/2$ and the pressure is plotted as function of the x coordinate in $L_y/2$.

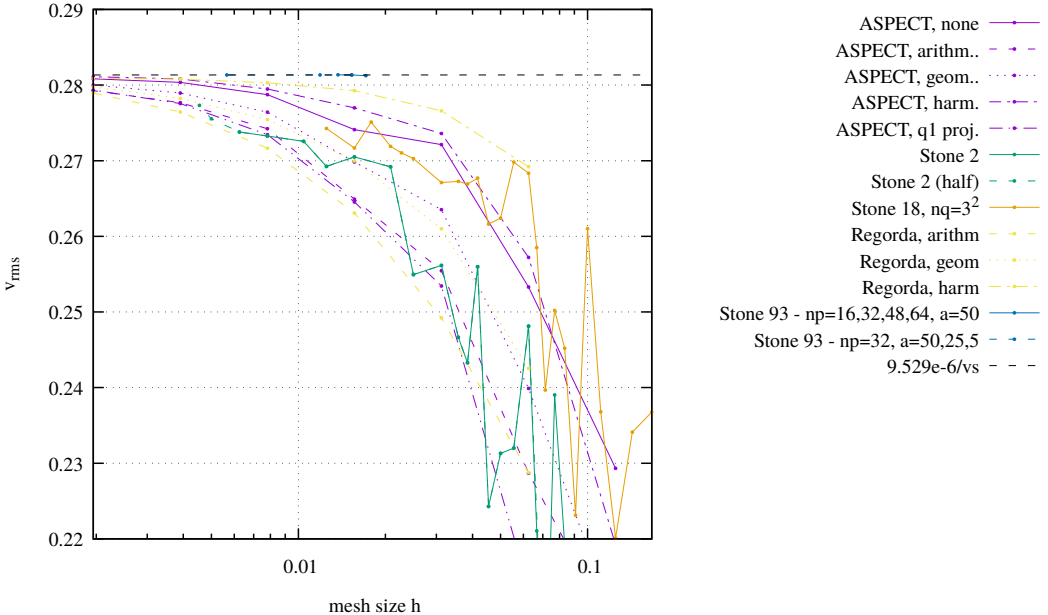


Figure 9: v_{rms} as function of element size for the instantaneous 2D sphere experiment in case of no slip boundary conditions and with different average schemes for the viscosity. Results are compared with results obtained by other numerical codes.

10.7 Rayleigh-Taylor instability

This problem has been originally presented by van Keken et al. (1997) and here it is performed as the isoviscous case (Case 1a). The domain has $L_x = 0.9142$ and $L_y = 1$ and gravity $\mathbf{g} = (0, -1)$. Two fluids with same constant viscosities ($\eta_1 = \eta_2 = 1$) and different densities ($\rho_1 = 1000$ and $\rho_2 = 1010$), with the lighter fluid at the bottom. The initial interface between the fluids is given by $y(x) = 0.2 + 0.02 \cos\left(\frac{\pi x}{L_x}\right)$. The experiment is performed with different grid sizes (50×50 , 80×80 , 100×100 and 256×256). A total of 1960000 markers are randomly distributed at the beginning of the simulation. Velocity boundary conditions are set to no slip at the top and the bottom, and to free slip at the sides of the domain.

v_{rms} as function of time is reported in Fig. 10, matching well with results shown by van Keken et al. (1997), Tackley and King (2003) and Thieulot (2014). Fig. 11 shows the evolution of the experiment at different time steps. All data can be found at https://github.com/aleregora/Benchmarks/tree/main/Momentum_equation/Rayleigh_Taylor_experiment/ISOVISCOUS.

10.8 Falling blocks

This benchmark is described as proposed by Gerya and Yuen (2003), Gerya (2010) and Thieulot (2011). The domain is square with $L_x = L_y = 500$ km and the grid is composed by 50×50 elements with 25 markers in each element. The block is initially centred at $(x = 250$ km; $y = 400$ km) and has a size of 100×100 km (Fig. 12a). The fluid surrounding the block has $\eta_f = 10^{21}$ Pa s $^{-1}$ and $\rho_f = 3200$ kg m $^{-3}$. The benchmark tests with different viscosities of the block, with η_b from 10^{15} Pa s $^{-1}$ to 10^{27} Pa s $^{-1}$. In each experiment also the density ρ_b of the block varies from 3220 kg m $^{-3}$ to 9900 kg m $^{-3}$. Velocity boundary conditions are set to free slip conditions on all sides of the domain. Density distributions at $t = 20$ Myr for $\rho_b = 3300$ kg m $^{-3}$ and different η_b are plotted in Fig. 12b-f, showing that the code correctly preserve the block geometry in case of large viscosity contrast, with a block stiffer than the surrounding fluid (Fig. 12f).

The velocity in the centre of the falling block at $t = 0$ is measured for all experiments and, since the velocity should increase with density contrast, the quantity $v/(\rho_b - \rho_f)$ is plotted as function of the viscosity contrast. All results perfectly match with those from Gerya (2010) and they line up on a single curve, demonstrating that the code can correctly deal with large viscosity and density contrasts (Fig. 13). All data can be found at https://github.com/aleregora/Benchmarks/tree/main/Momentum_equation/Falling%20blocks.

10.9 2D time-dependent Stokes sphere with deformable free surface

This experiment is performed in a unit square domain with the gravity acceleration fixed to $g_y = -1$. The sphere has $\rho_s = 2$ and $\eta_s = 10^3$ and is initially centred at $(0.5; 0.6)$ with radius $R = 0.123456789$. The fluid surrounding the sphere

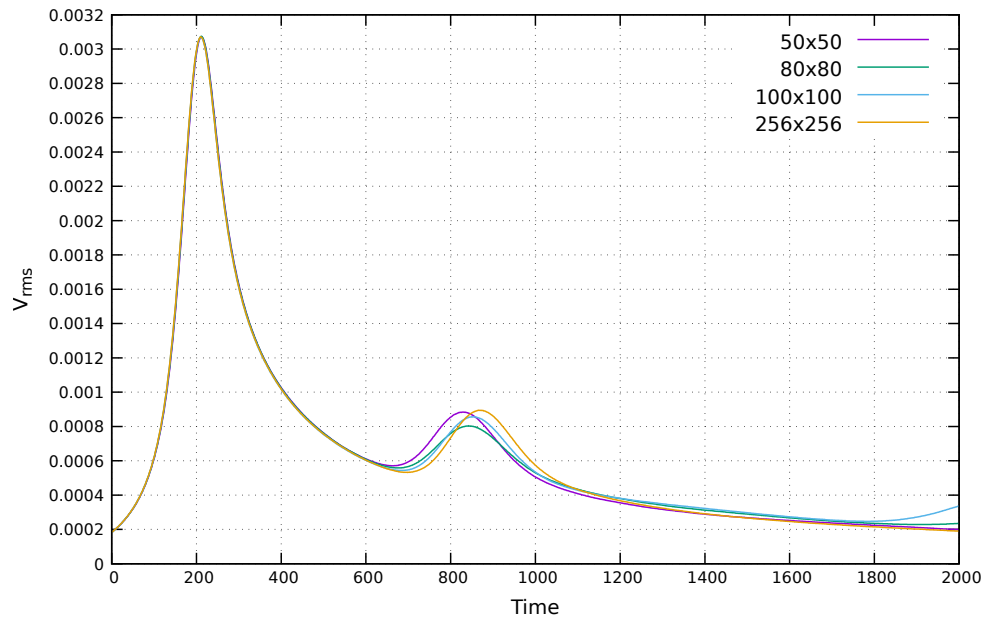


Figure 10: v_{rms} of the Rayleigh-Taylor experiment as function of time for different resolution of the grid.

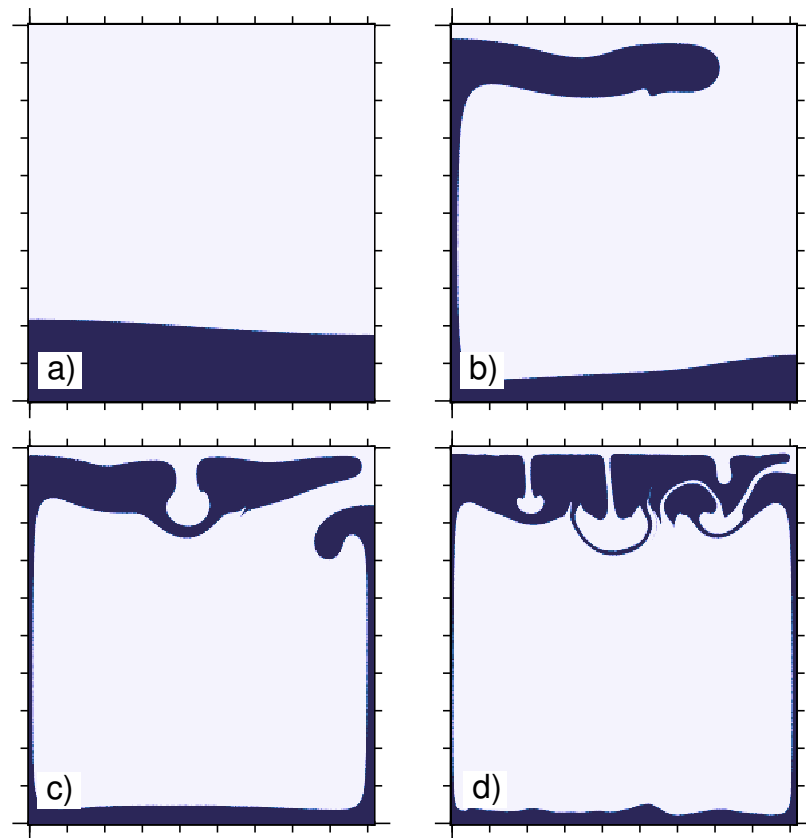


Figure 11: Evolution of the Rayleigh-Taylor experiment for a grid of 256×256 elements at $t = 0, 500, 1000$ and 2000 (panels a, b, c and d, respectively).

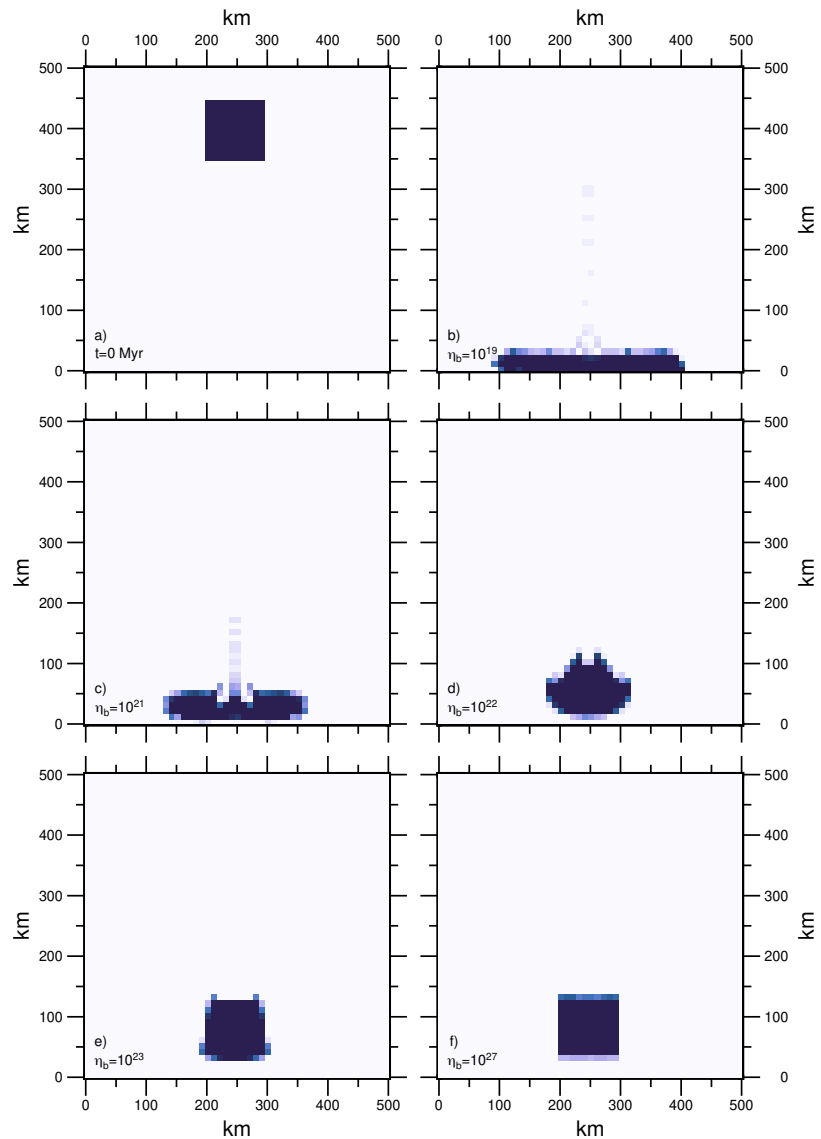


Figure 12: Density evolution of the falling block experiment at $t = 0$ Myr (panel a) and $t = 20$ Myr for different viscosities of the block (panels b-f).

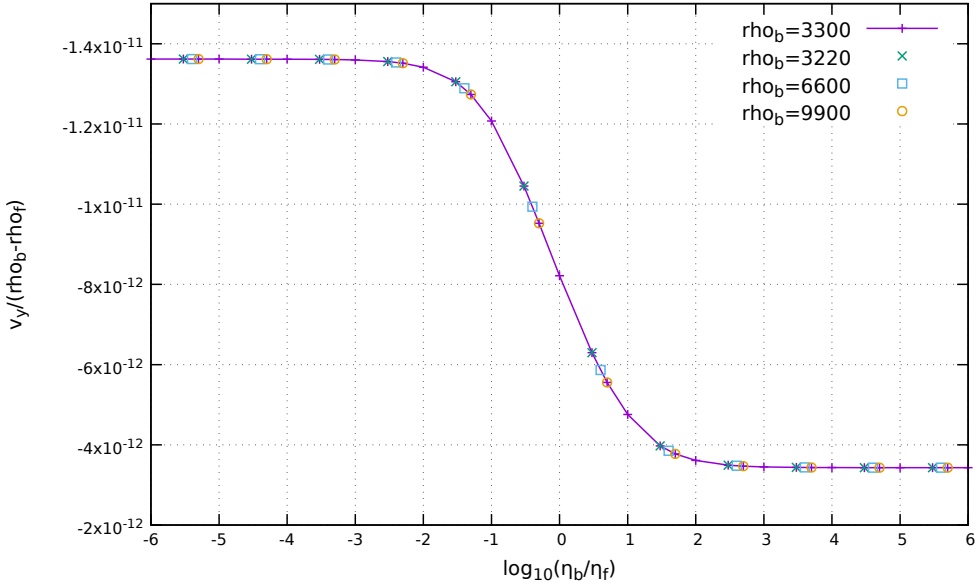


Figure 13: Initial velocity relative to the density contrast at the centre of the falling block as function of the viscosity contrast between the block and the surrounding fluid.

has $\rho_f = 1$ and $\eta_f = 1$ and occupies the domain for $y \leq 0.75$, while for $y > 0.75$ the air has $\rho_a = 0$ and $\eta_a = 10^{-3}$. Velocity boundary conditions are set to free slip on all sides. The Courant number is set to 0.25. The experiments run for 200 s using grid resolutions from 150×150 to 512×512 elements, with 25 randomly distributed markers per element, and for different average schemes for the viscosity. The interface between the fluid and the air is tracked by means of the markers chain. Results in terms of velocity and pressure fields and topography variations are compared with results obtained with ASPECT (Kronbichler et al., 2012; Heister et al., 2017; Bangerth et al., 2020a,b) and they can be found at https://github.com/cedrict/fieldstone/tree/master/images/stokes_sphere_fs2D and https://github.com/aleregora/Benchmarks/tree/main/Surface_processes/Time_dependent_sphere. Results in terms of the v_{rms} in case of an arithmetic average are also shown in Fig. 14.

10.10 Free surface stabilisation

The benchmark is performed as discussed in Kaus et al. (2010) and Thieulot (2014). The domain is square with $L_x = L_y = 500$ km and a grid resolution of 200×200 elements, each of them containing 16 markers. A buoyant fluid with $\rho_1 = 3200 \text{ kg m}^{-3}$ and $\eta_1 = 10^{20} \text{ Pa s}$ is overlain by a denser fluid with $\rho_2 = 3300 \text{ kg m}^{-3}$ and $\eta_2 = 10^{21} \text{ Pa s}$. The initial interface between the fluids has an initial sinusoidal shape of 5 km amplitude. Velocity boundary conditions are set to free slip conditions at the sides and no slip at the bottom, while the top is free surface. The experiment is performed with various fixed time steps, without the use of the Courant number. The vertical position of the free surface at $x = L_x$ is tracked for each simulation, with or without the stabilisation algorithm.

The results show an instability (drunken sailor effect) increasing the time step in case that the stabilisation algorithm is not activated ($dt = 4200$ yr, green line in Fig. 15), as already observed by Kaus et al. (2010) and Thieulot (2014). Activating the algorithm the instability is fixed and the simulation remains stable using time step up to 50 000 yr (red line in Fig. 15). All data can be found at https://github.com/aleregora/Benchmarks/tree/main/Surface_processes/Stabilisation_algorithm.

10.11 Topography relaxation

This experiment is performed as in Crameri et al. (2012) using free surface and sticky air (Case 1). The domain is rectangular with $L_x = 2800$ km and $L_y = 700$ km in case of free surface and $L_y = 800$ km in case of sticky air ($h_{st} = 100$ km). The grid is composed by 256×64 elements for the free surface 560×320 elements for the sticky air. For both cases, there is a mantle of 600 km thickness with $\eta_m = 10^{21} \text{ Pa s}$ overlain by a highly viscous cosine-shaped lithosphere with thickness between 93 and 107 km and $\eta_l = 10^{23} \text{ Pa s}$. Both mediums have $\rho = 3300 \text{ kg m}^{-3}$. In case of sticky air experiment, the air has $\rho_a = 0 \text{ kg m}^{-3}$ and $\eta_a = 10^{18} \text{ Pa s}$. The gravity acceleration is set to $g_y = -10 \text{ m s}^{-2}$. Velocity boundary conditions are set to no slip at the bottom and free slip at the sides of the domain. In case of sticky air, velocities on top are set to free slip conditions.

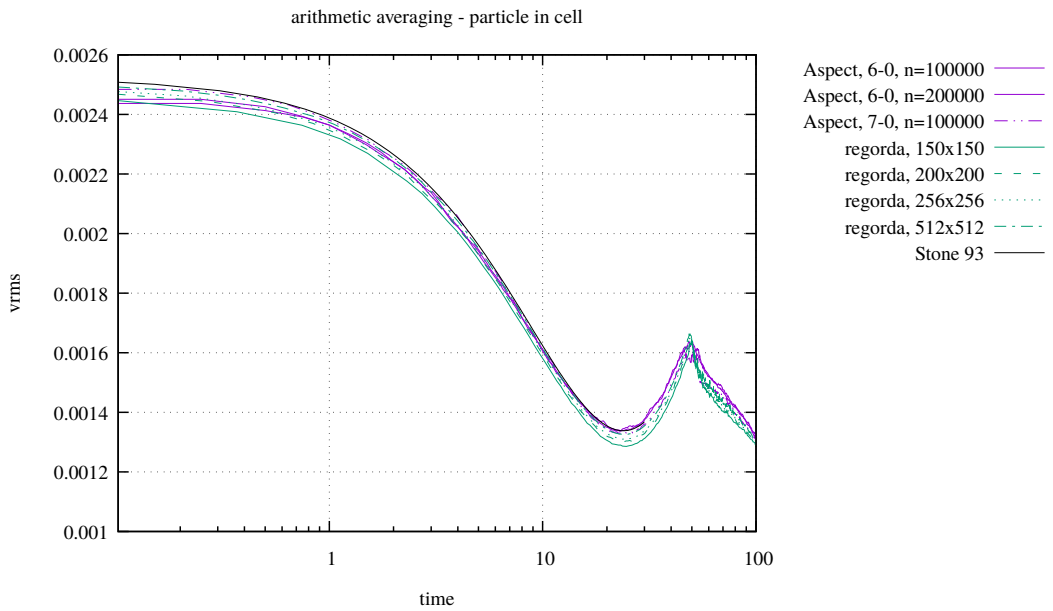


Figure 14: v_{rms} for different grid resolutions as function of time for the 2D time-dependent Stokes sphere experiment in case of an arithmetic average. Results are compared with results obtained by ASPECT.

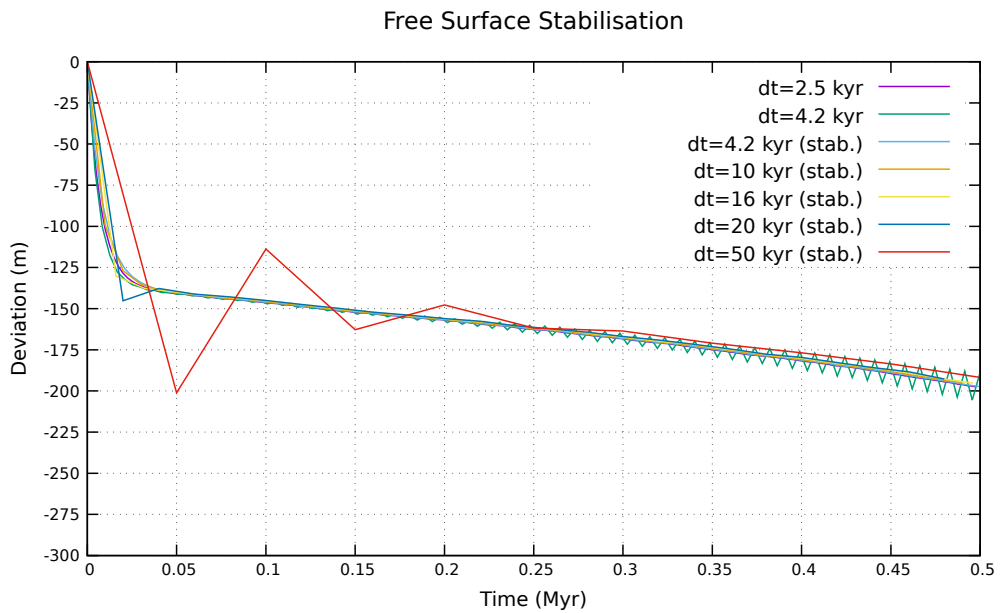


Figure 15: Evolution of the y coordinate in $x = L_x$ as function of time for different time steps, with and without the stabilisation algorithm.



Figure 16: Maximum topography as function of time for the Crameri benchmark (coloured lines) in comparison with the analytical solution (black line) and results obtained with UNDERWORLD (yellow line) and SULEC (blue line).

The maximum topography as function of time ($h(t)$) can be analytically derived in according to

$$h(t) = h_0 \exp(\gamma t)$$

where $h_0 = 7$ km is the initial topography, $\gamma = -0.2139 \times 10^{-11}$ is the characteristic relaxation rate and t is the time (black line in Fig. 16). Maximum topography at the characteristic relaxation time $t_{rlx} = 14.825$ kyr can be found to be $h_{rlx} = 2576$ m. The results show that a viscosity of the air of 10^{18} Pas is needed in case of $h_{st} = 100$ km to correctly describe the topography relaxation for this problem, as pointed out by Crameri et al. (2012) (purple line in Fig. 16). The case with a true free surface well follows the analytical solution (orange line in Fig. 16). In particular, at the relaxation time in case of the true free surface predicts a maximum topography of 2570 m, with an error of 6 m with respect to the analytical solution. Results are also compared with results obtained with a free surface in UNDERWORLD (256×64 elements) and SULEC (401×201 elements) (with courtesy from Crameri et al., 2012). All data can be found at https://github.com/aleregora/Benchmarks/tree/main/Surface_processes/Topography_relaxation.

10.12 Spontaneous subduction

This experiment is performed as presented by Schmeling et al. (2008), in case of both a sticky air and a true free surface and using different average schemes for the viscosities. The domain is rectangular with $L_x = 3000$ km and $L_y = 700$ km, a grid resolution of 256×64 elements with 50 markers per element and Courant number of 0.01. At the beginning of the simulation, a 100 km-thick lithospheric layer with $\rho_m = 3300 \text{ kg m}^{-3}$ and $\eta_m = 10^{23}$ Pas is located at the top of the domain for x between 1000 and 3000 km, while the asthenospheric mantle has $\rho_m = 3200 \text{ Pa s}$ and $\eta_m = 10^{21}$ Pas. In addition, a 200 km-depth lithospheric slab is already subducted in the mantle in order to have a spontaneous subduction. In case of sticky air, $L_y = 750$ km and a 50 km-thick air layer with η_a from 10^{19} Pas to 10^{21} Pas overlie the mantle. Velocity boundary conditions are set to free slip on the sides and on the bottom of the domain. In case of sticky air, velocities on the top boundary are set to free slip conditions as well.

The maximum depth of the slab is tracked for all the simulations (Fig. 17) and they are compared with results obtained by Schmeling et al. (2008) with models with regular grids and comparable grid resolutions (rectangles in Fig. 17). Low viscous sticky air models (i.e., 10^{19} Pas) enlighten a strong dependence of the sinking velocity with the chosen average scheme (dashed lines in Fig. 17), while high viscous sticky air models (i.e., 10^{21} Pas) show a higher resistance at the trench, underestimating the correct solution (dotted lines in Fig. 17). A high resistance at the trench can be also observed in case of a true free surface for the low resolution grid used (continuous lines in Fig. 17), as pointed out by Schmeling et al. (2008). All data can be found at https://github.com/aleregora/Benchmarks/tree/main/Surface_processes/Spontaneous_subduction.

10.13 The slab detachment

The slab detachment benchmark is performed as described by Schmalholz (2011) and Glerum et al. (2018). The domain is rectangular with $L_x = 1000$ km and $L_y = 660$ km and a grid resolution of 256×256 elements. A non-linear viscous T-shaped layer with $\rho_l = 3300 \text{ kg m}^{-3}$ is placed at the top of the domain and surrounded by a linear viscous

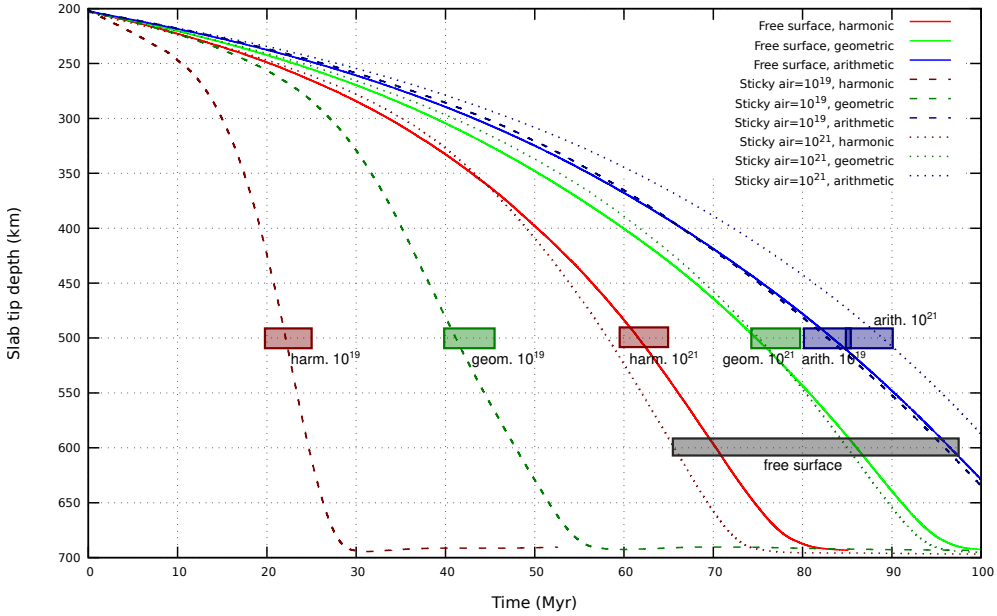


Figure 17: Maximum depth of the slab as function of time for all the simulations of the Schmeling et al. (2008) benchmark, in case of harmonic, geometric and arithmetic means (red, green and blue lines, respectively) using a sticky air or a true free surface (discontinuous and continuous lines, respectively). Red, green and blue rectangular areas indicate the range of times from Schmeling et al. (2008) when the slab tip reaches 500 km in case of sticky air, while the grey rectangular area indicates the range of times from Schmeling et al. (2008) when the slab tip reaches 600 km in case of true free surface.

fluid with $\rho_f = 3150 \text{ kg m}^{-3}$. The top layer is 80 km-thick and a 250 km-long and 80 km-wide slab is placed at $x = L_x/2$ (Fig. 18a). The effective viscosity of the top layer is given by

$$\eta_{eff} = \eta_0 I_2^{\frac{(1-n)}{n}}$$

with $\eta_0 = 4.75 \times 10^{11} \text{ Pas}$ and $n = 4$, while the surrounding fluid has $\eta_f = 10^{21} \text{ Pas}$. The effective viscosity is capped between $\eta_{min} = 10^{21} \text{ Pas}$ and $\eta_{max} = 10^{25} \text{ Pas}$. Velocity boundary conditions are set to free slip at the top and the bottom, and to no slip at the sides of the domain.

The sinking of the slab determines a decrease of the effective viscosity in the T-shaped layer during the first part of the evolution (Fig. 18a), as consequence of local strain rates, while effective viscosities increase up to η_{max} in the top layer after approximately 20 Myr, when necking is complete (Fig. 18b).

The width of necking is tracked by means of markers position at the side of the slab. Necking width and time are normalised in function of the initial slab (80 km) and the characteristic time ($t_c = 7.1158 \times 10^{14} \text{ s}$) (Schmalholz, 2011; Glerum et al., 2018). The results in case of arithmetic, geometric and harmonic mean of the viscosity are shown in Fig. 19, compared with results from Glerum et al. (2018) for which an infinity norm mean was used. The influence of the average schemes agrees with results shown in Section 10.12. All data can be found at https://github.com/aleregorde/Benchmarks/tree/main/Nonlinear_visco_plasticity/Slab_detachment.

10.14 The indenter experiment

The indenter benchmark simulate a rigid punch on a purely plastic von Mises material, for which exists an analytical solution (Thieulot et al., 2008; Thieulot, 2014; Glerum et al., 2018). The domain is a unit square with a grid resolution of 256×256 elements. The gravity acceleration is set to $\mathbf{g} = \mathbf{0}$ and effective viscosity is capped using $\eta_{min} = 10^{-4}$ and $\eta_{max} = 10^3$. The tolerance for the convergence of the non-linear solution is $tol = 10^{-9}$, with a maximum number of non-linear iterations set to 500. The medium in the domain has $\rho = 0.01$, an initial viscosity $\eta_0 = 10$, cohesion $C = 1$ and an angle of internal friction $\phi = 0^\circ$. Velocity boundary conditions are set to no slip at the bottom and free slip at the sides of the domain. The top of the domain is open with the exception of the central portion (punch area) with width $w_p = 0.125$, where $v = -1.05$ and u is fixed either to 0 (rough punch experiment) or free (smooth punch experiment).

Fig. 20 show the results in terms of viscosity (panels a and b), strain rate (panels c and d), velocity (panels e and f) and pressure (panels g and h) for both experiments. The analytical solution indicate that pressure at $(0.5; 1)$ and $(0.5 \pm w_p; 1)$ is $p = \pi + 1$ and $p = 1$, respectively (black and red lines in Fig. 21). Fig. 21 shows a clear

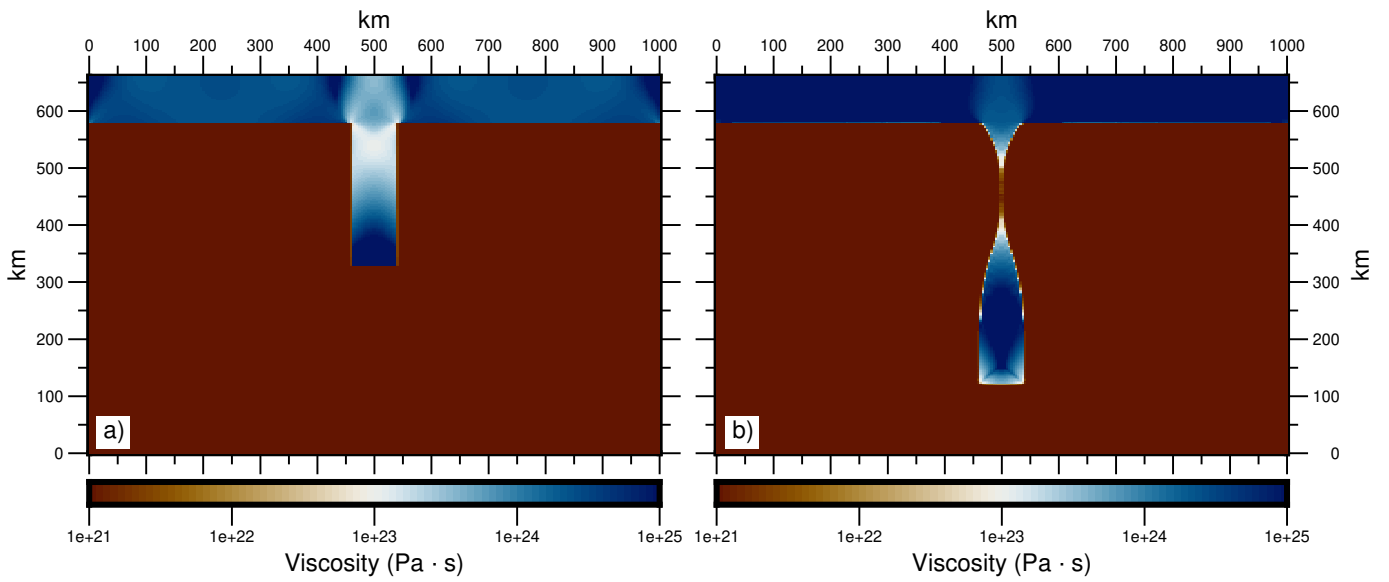


Figure 18: Effective viscosity for the slab detachment benchmark at the beginning of the evolution (panel a) and when necking is complete (panel b).

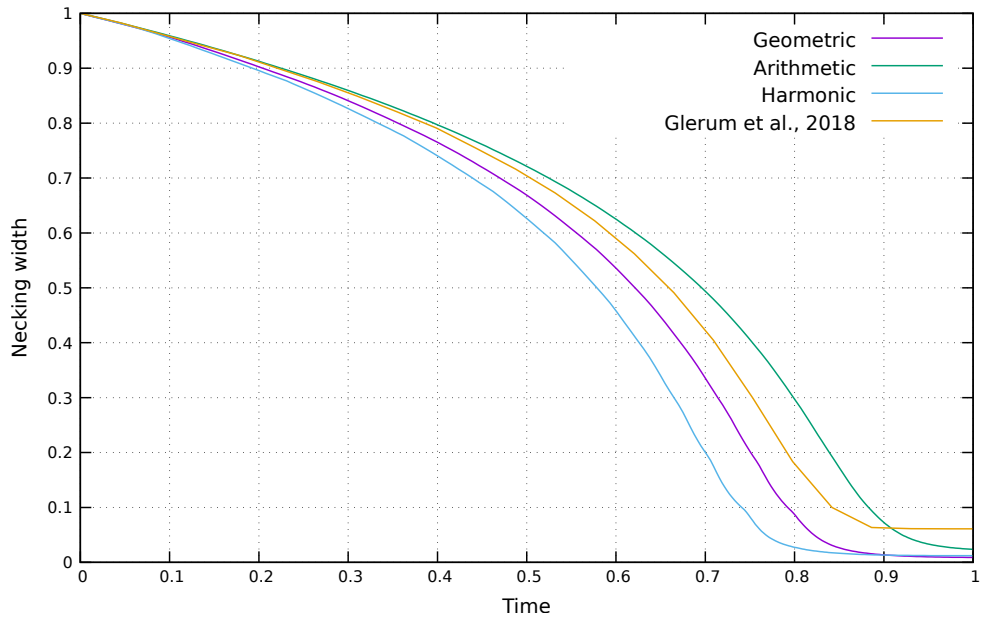


Figure 19: Normalised width of the necking of the slab detachment benchmark as function of normalised time.

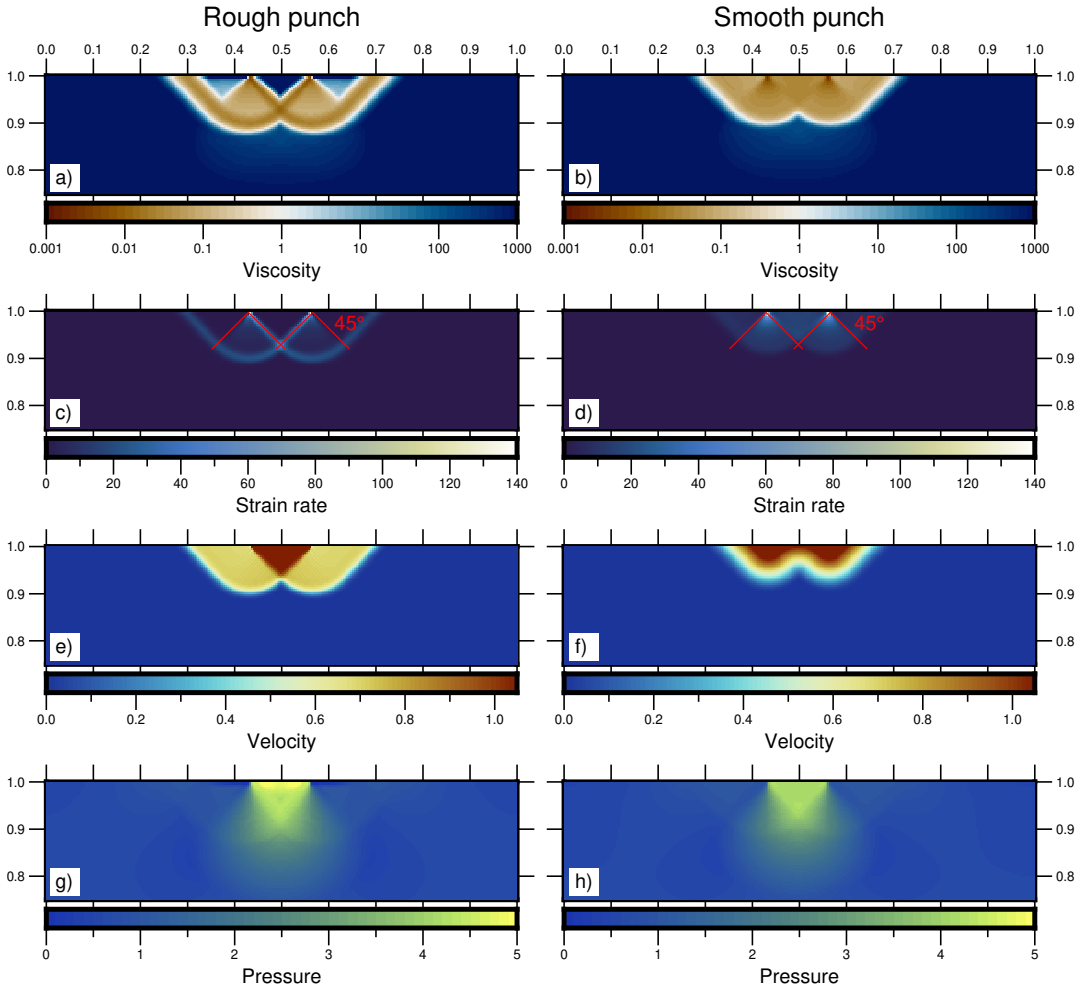


Figure 20: Viscosity (panels a and b), strain rate (panels c and d), velocity (panels e and f) and pressure (panels g and h) fields for rough (left column) and smooth (right column) punch experiments.

improvement in the pressure solution when passing from a rough to a smooth punch (green and blue lines in Fig. 21, respectively), as previously observed by Thieulot (2014) and Glerum et al. (2018). All data can be found at https://github.com/aleregorde/Benchmarks/tree/main/Nonlinear_visco_plasticity/Indenter.

10.15 The brick experiment

An instantaneous version of the brick benchmark is performed to verify the correctness of the pressure-dependent plasticity for different angle of internal friction, as proposed by Glerum et al. (2018). The domain is rectangular with $L_x = 40$ km and $L_y = 10$ km and a grid resolution of 512×128 elements. The gravity acceleration is set to $g_y = -10$ m s $^{-2}$ and effective viscosity is capped using $\eta_{min} = 10^{19}$ Pa s and $\eta_{max} = 10^{26}$ Pa s. The tolerance for the convergence of the non-linear solution is $tol = 10^{-7}$, with a maximum number of non-linear iterations set to 1000. A 800 m-wide and 400 m-height inclusion with $\eta_b = 10^{20}$ Pa s and $\rho_b = 2700$ kg m $^{-3}$ is placed at the bottom of the domain at $x = L_x/2$. The inclusion is surrounded by a non-linear viscous medium with $\rho_m = 2700$ kg m $^{-3}$, an initial viscosity of 10^{23} Pa s, a linear viscous viscosity of 10^{25} Pa s and a cohesion of 40 MPa. Velocities are set to free slip conditions at the bottom of the domain and the top is open. Velocities on sides of the domain are fixed to $u = \pm 2 \times 10^{-11}$ m s $^{-1}$ and $v = 0$. The experiment is performed in compressional and extensional contexts with an angle of internal friction ϕ of the non-linear medium variable between 0° and 30° .

As expected, two shear bands stem from the inclusion with variable angles in relation to both the dynamics context and the internal friction angle. Shear band angles formed at 45° for $\phi = 0^\circ$ in both extensional and compressional contexts (Fig. 22a), while they are different in case of $\phi \neq 0^\circ$. Shear band angles in case of $\phi = 20^\circ$ are shown for compression and extension in Fig. 22b and c, respectively. Values of shear band angles as function of internal friction angles from 0° to 30° are extracted at different depths and minimum and maximum values are plotted in Fig. 23, in comparison with theoretical Roscoe, Arthur and Coulomb shear band angles. For all tests the tolerance for nonlinear convergence is defined $tol = 10^{-7}$ and none converges before the maximum number of iterations ($it_{max} = 1000$) is reached. However, tests with internal friction angles up to 15° show a constant decrease of the velocity residuals,

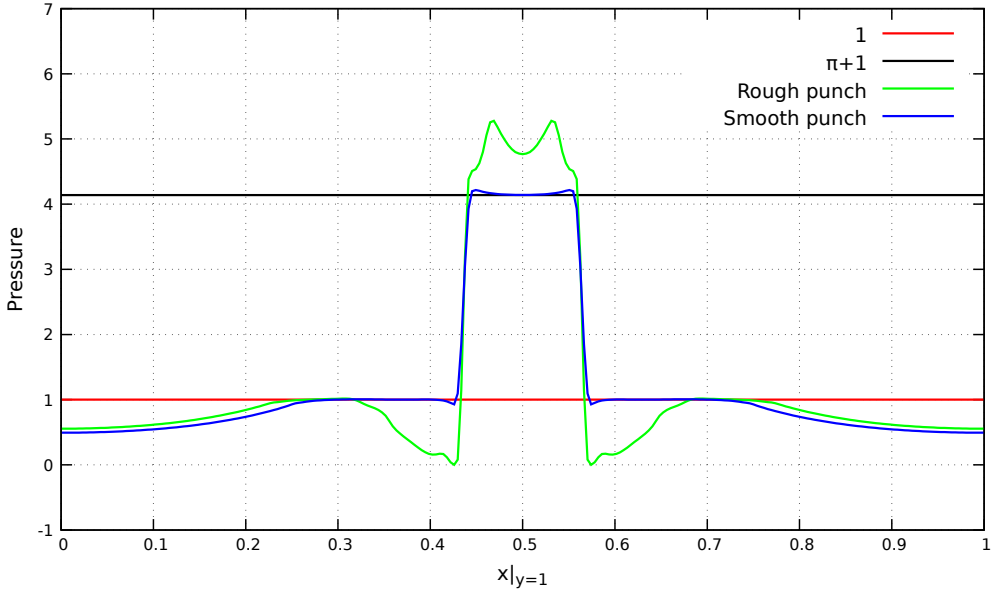


Figure 21: Nodal pressure in function of the x coordinate at $y = 1$ for rough (green line) and smooth (blue line) punch experiment. Black and red lines indicate the analytical solution at $x = 0.5$ and $x = 0.5 \pm w_p$, respectively.

which can not be observed for for tests with higher internal friction angles (Fig. 24). All data can be found at https://github.com/aleregora/Benchmarks/tree/main/Nonlinear_visco_plasticity/Brick_experiment.

10.16 Advection stabilisation

The 1D advection problem proposed by [Donea and Huerta \(2003\)](#) and [Thieulot \(2011\)](#) is performed to verify the effectiveness of the SUPG method to stabilise the advection term of the energy equation. The domain is a 1D segment with $L_x = 1$ composed by 50 elements and a discontinuity in the thermal field placed at $x = 0.25$. Temperature is set to 1 for $x \leq 0.25$ and to 0 for $x > 0.25$. Velocity is set to $u = 1$ in the entire domain. The simulation is performed for 250 time steps, with $dt = 0.002$, so the thermal discontinuity should be at $x = 0.75$ at the end of the simulation.

Temperature profiles at the end of the simulation are shown in 25 as function of the dimensionless coefficient $\gamma = \tau v/h$. In case of the classic Galerkin method ($\gamma = 0$, blue line in 25) the final thermal profile is characterised by strong oscillations, which are eliminated in case of the SUPG method ($\gamma = 0.045$, orange line in 25). All data can be found at https://github.com/aleregora/Benchmarks/tree/main/Energy_equation/Advection_stabilisation.

10.17 Shear heating

This exercise is performed in an unit square domain composed by 128×128 elements. The velocity field is prescribed on the entire domain with $\mathbf{v} = (L_y - y)\mathbf{e}_x$; viscosity, density and specific heat are fixed to 1, while thermal conductivity and radiogenic energy are fixed to 0. Therefore, the energy equation (Eq. 3) can be simplified as

$$\frac{\partial T}{\partial t} = H_s$$

and fixing $T(t = 0) = 0$, the temperature can be find as

$$T(t) = H_s t$$

In this case we have

$$\begin{aligned}\dot{\epsilon}_{xx} &= \frac{\partial u}{\partial x} = 0 \\ \dot{\epsilon}_{yy} &= \frac{\partial v}{\partial y} = 0 \\ \dot{\epsilon}_{xy} &= \frac{1}{2} \left(\frac{\partial v}{\partial x} + \frac{\partial u}{\partial y} \right) = \frac{1}{2}(L_y - 2y)\end{aligned}$$

and, simplifying Eq. 24, shear heating can be calculated as

$$H_s(x, y) = (1 - 2y)^2$$

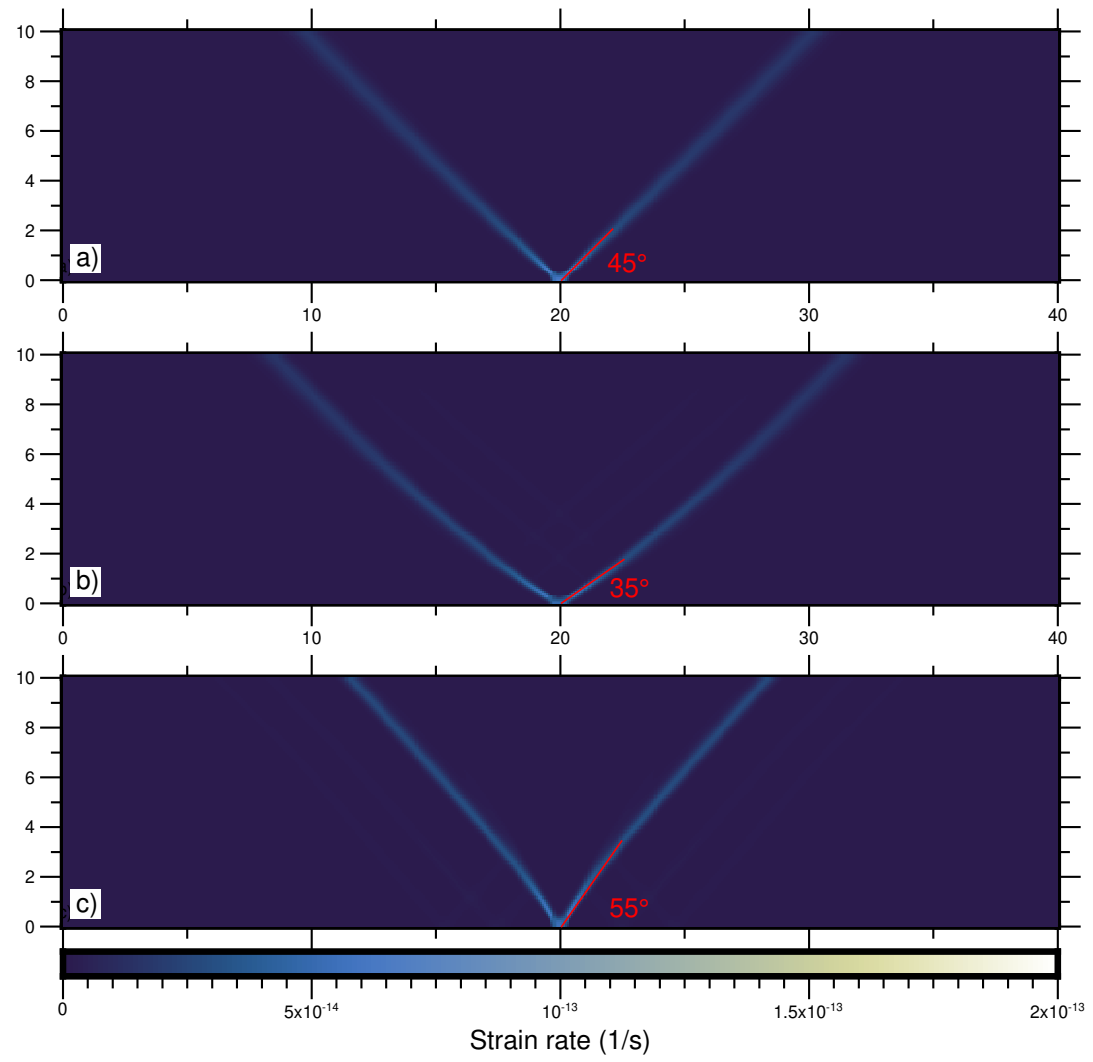


Figure 22: Shear band angles predicted for the brick experiment for $\phi = 0^\circ$ (panel a) and for $\phi = 20^\circ$ in case of compression and extension (panels b and c, respectively).

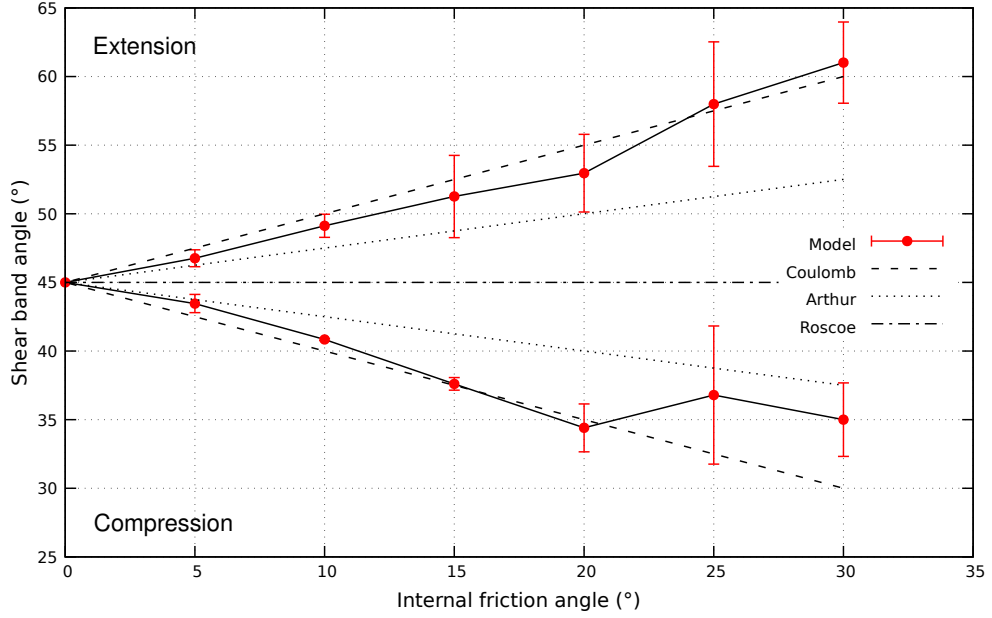


Figure 23: Shear band angles predicted for the brick experiment in case of compressional and extensional contexts as function of different internal angle of friction (continuous black line and red dots), compared with theoretical Roscoe, Arthur and Coulomb angles (discontinuous black lines). Red lines indicate the range of angles calculated at different depths.

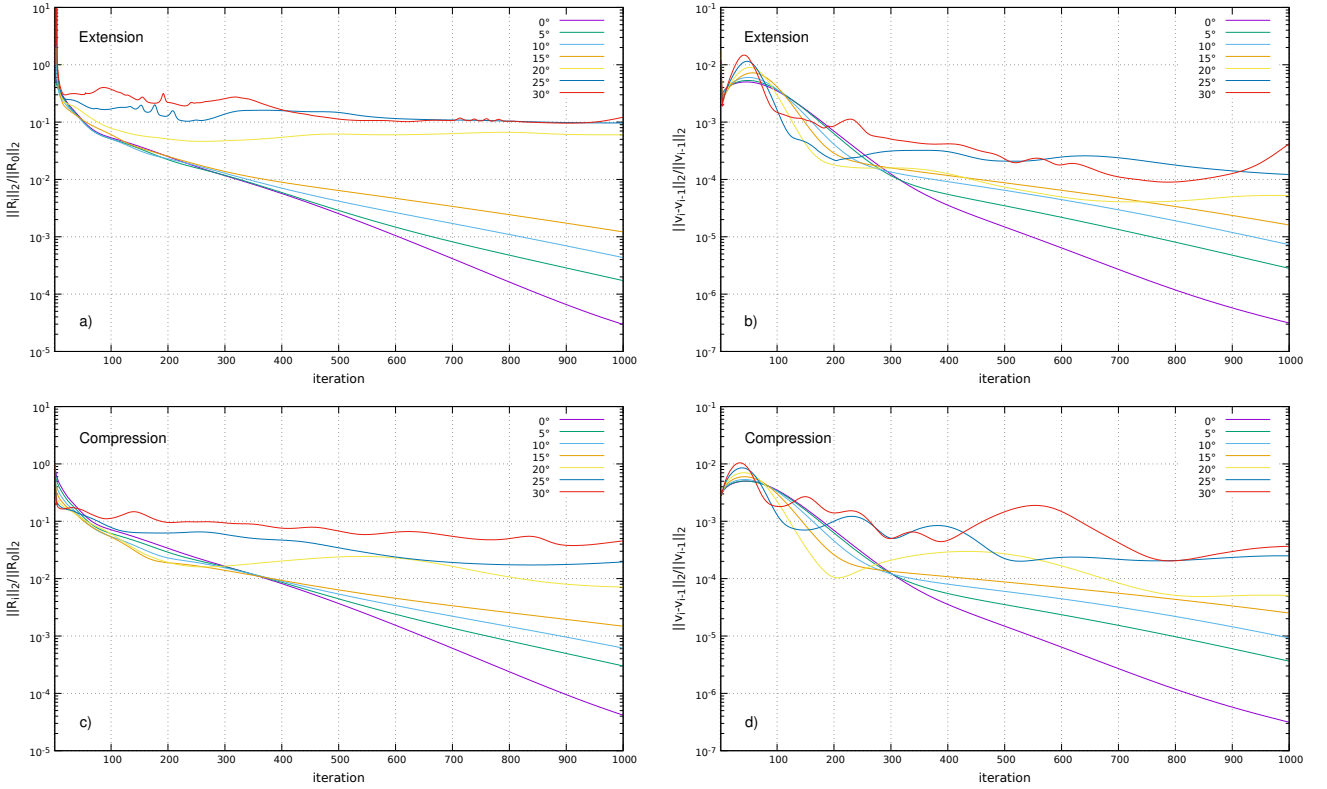


Figure 24: Convergence rates for all tests. Normalised residuals (left column) are compared with velocity residuals (right column) for extensional (first row) and compressional (second row) settings.

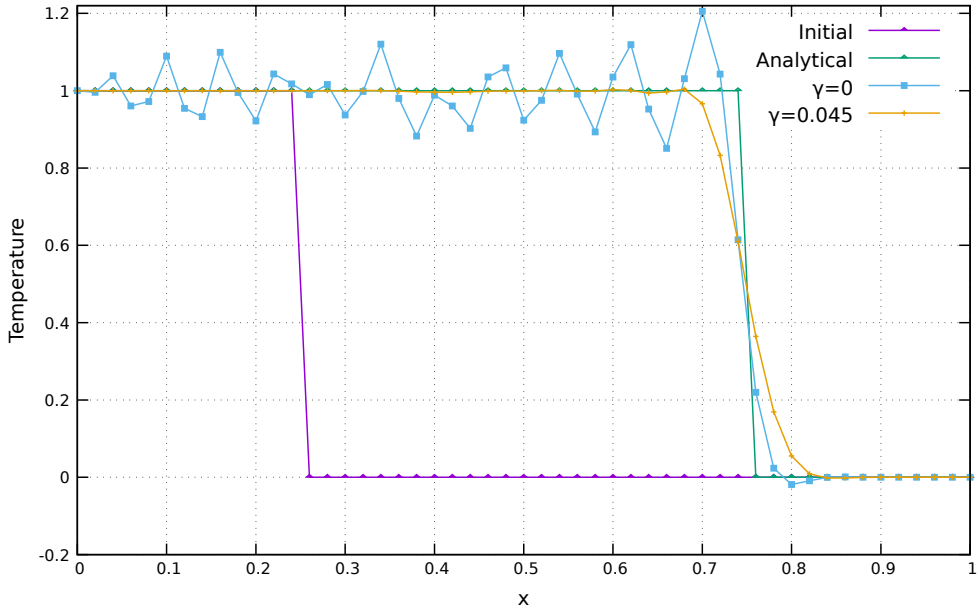


Figure 25: Temperature profile as function of x for the advection stabilisation benchmark. Purple line indicates the initial temperature profile; the green line indicates the analytical temperature profile after 250 time steps; blue line indicates the temperature profile after 250 time steps in case of the classic Galerkin method ($\gamma = 0$); orange line indicates the temperature profile after 250 time steps in case of the SUPG method ($\gamma = 0.045$).

The solution predicted by the model in terms of velocity, temperature and shear heating match well with the analytical solutions (Fig. 26). All data can be found at https://github.com/aleregora/Benchmarks/tree/main/Energy_equation/Simple_shear.

10.18 Shear and adiabatic heating

This problem is performed as presented in Exercise 9.4 in Gerya (2010). Two materials are vertically separated in a rectangular domain with $L_x = 1000$ km, $L_y = 1500$ km and a grid resolution of 30×20 elements. Constant thermal coefficient expansion ($\alpha = 3 \times 10^{-5} \text{ K}^{-1}$), temperature ($T = 1300 \text{ K}$) and gravity acceleration ($g_y = -10 \text{ m s}^{-2}$) are assumed in the whole domain. Fluid 1 (on the left side of the domain) has $\rho_1 = 3200 \text{ kg m}^{-3}$ and $\eta_1 = 10^{20} \text{ Pas}$; fluid 2 (on the right side of the domain) has $\rho_2 = 3300 \text{ kg m}^{-3}$ and $\eta_2 = 10^{22} \text{ Pas}$. Velocity boundary conditions are set to free slip on all sides of the domain.

As shown in Fig. 27, both shear and adiabatic heating predicted by the code (first row in Fig. 27) well recreate the results obtained by means of example *Shear_adiabatic_heating.m* from Gerya (2010) (second row in Fig. 27). All data can be found at https://github.com/aleregora/Benchmarks/tree/main/Energy_equation/Adiabatic%2BShear.

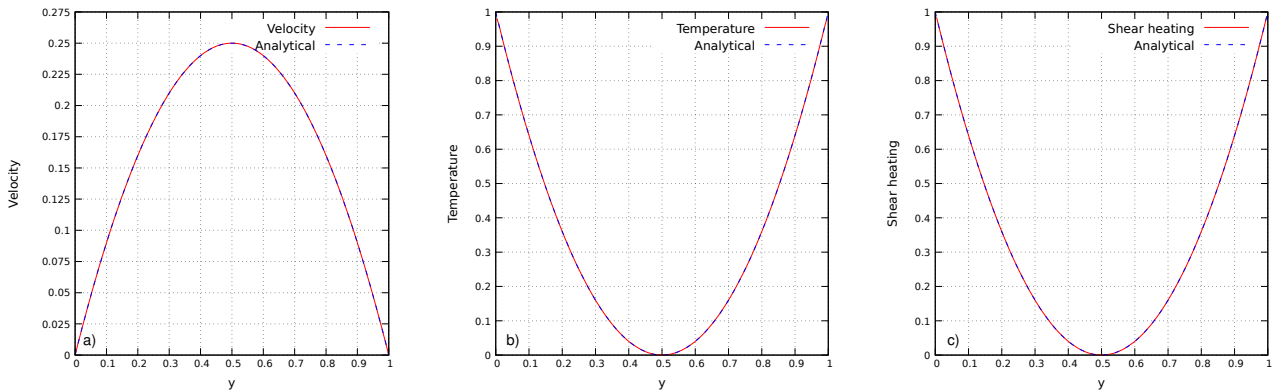


Figure 26: Velocity (panel a), temperature (panel b) and shear heating (panel c) as function of the y coordinate for the simple shear experiment. The solutions predicted by the model (red lines) are compared with the analytical solutions (dashed blue lines).

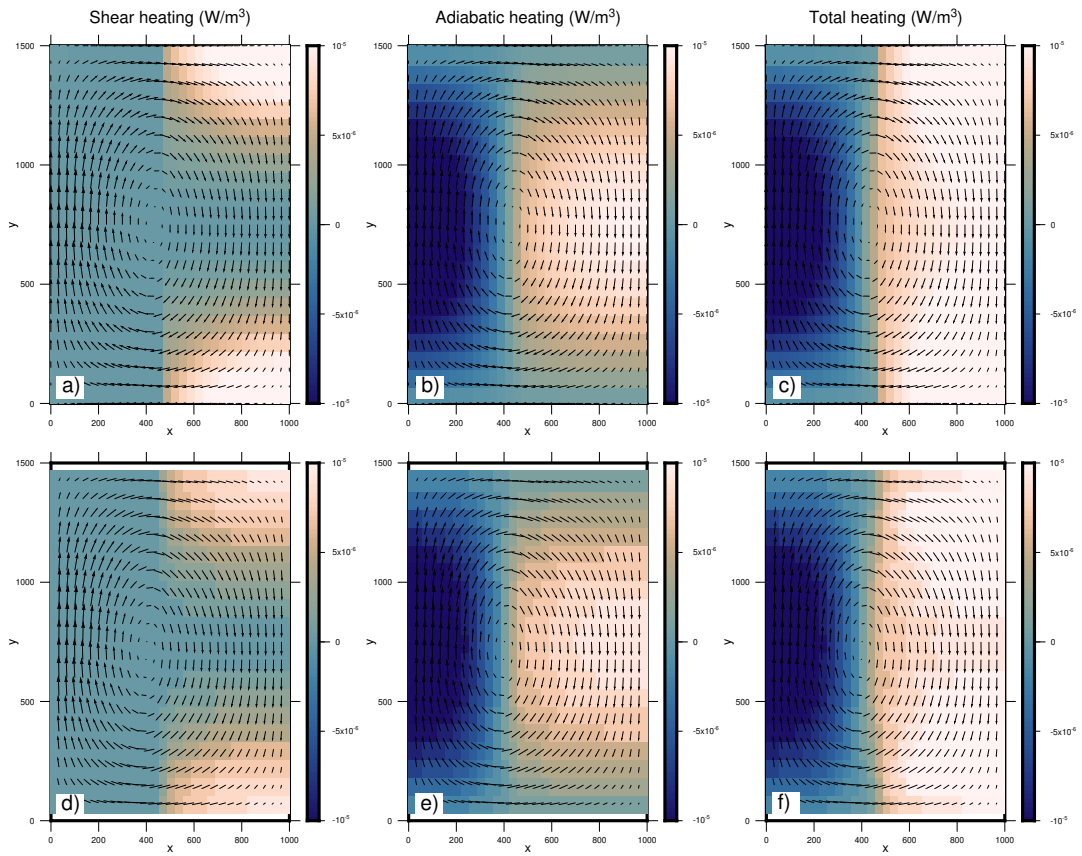


Figure 27: Comparison between shear (first column), adiabatic (second column) and total (third column) energy predicted by the code (panels a, b and c) and those created using example *Shear_adiabatic_heating.m* from Exercise 9.4 in [Gerya \(2010\)](#) (panels d, e and f).

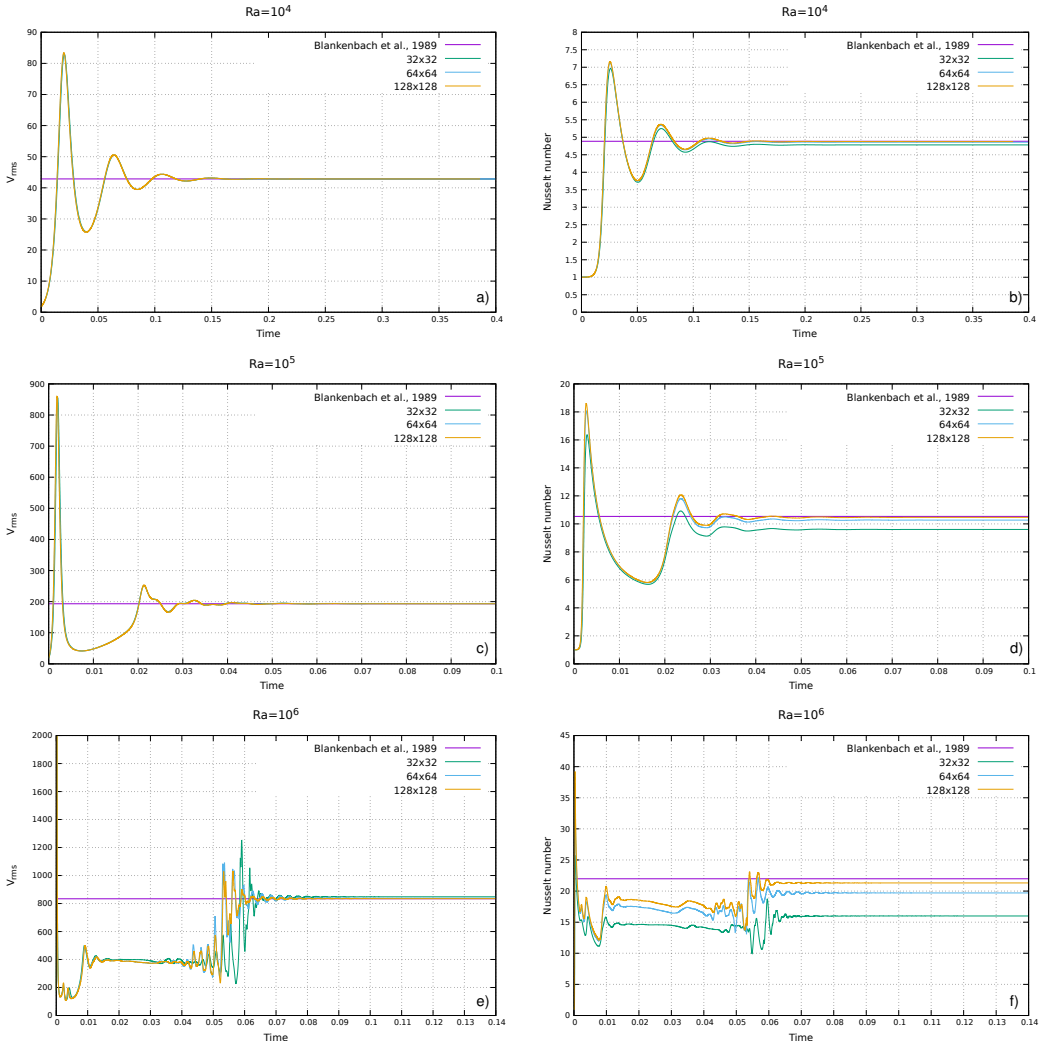


Figure 28: v_{rms} (panels a, c and e) and Nu (panels b, d and f) for the mantle convection benchmark as function of time for different grid resolution. Panels a and b show the results for $Ra = 10^4$; Panels c and d show the results for $Ra = 10^5$; panels e and f show the results for $Ra = 10^6$. Purple lines indicate the convergence values for the v_{rms} and the Nu from [Blankenbach et al. \(1989\)](#) at the steady state.

10.19 Mantle convection

This problem is performed as presented by [Blankenbach et al. \(1989\)](#) (constant viscosity cases) and [Thieulot \(2014\)](#), in a 2D unit square domain with gravity acceleration $g_y = 10^{10} Ra$. The experiment is performed with three different Rayleigh numbers ($Ra = 10^4, 10^5$ and 10^6) and with different grid resolution (between 32×32 and 128×128 elements). The fluid has constant viscosity, initial density, heat capacity, thermal conductivity ($\eta = \rho_0 = C_p = k = 1$), reference temperature ($T_0 = 0$) and thermal expansion coefficient ($\alpha = 10^{-10}$). Temperatures are set to 0 on top and 1 on bottom of the domain. Velocity boundary conditions are set to free slip on all sides. The initial temperature field is given by

$$T(x, y) = (1 - y) + 0.01 \cos(\pi x) \sin(\pi y)$$

The solution generated by the code in terms of v_{rms} (calculated as in Sec. 10.1) and Nu as function of time are reported for all the simulations in Fig. 28. At the steady state, v_{rms} and Nu of all simulations converge well toward the values from [Blankenbach et al. \(1989\)](#), with lower errors for higher resolution grids (Table 2). All data can be found at https://github.com/aleregorde/Benchmarks/tree/main/Momentum%2BEnergy/Mantle_convection.

		Blankenbach et al. (1989)	Thieulot (2014) 200 × 200	32 × 32	FALCON 64 × 64	128 × 128
$Ra = 10^4$	v_{rms}	42.864947 ± 0.000020	42.867	42.83226	42.852793	42.861394
	Nu	4.884409 ± 0.000010	4.882	4.781297	4.857475	4.877573
$Ra = 10^5$	v_{rms}	193.21454 ± 0.000010	193.255	193.872643	193.377472	193.252290
	Nu	10.534095 ± 0.000010	10.507	9.602514	10.270735	10.465629
$Ra = 10^6$	v_{rms}	833.98977 ± 0.000020	834.712	848.091176	837.767911	834.945793
	Nu	21.972465 ± 0.000020	21.695	15.999266	19.703682	21.306939

Table 2: Comparison between v_{rms} and Nu predicted by the code for the mantle convection experiment and same values as reported in literature.

10.20 Viscoplastic mantle convection

This benchmark is performed as Cases 1-5a described in Tosi et al. (2015) in a 2D unit square domain with two different grid resolutions of 32×32 and 100×100 elements. Reference viscosity, reference density, heat capacity, thermal conductivity and thermal expansion coefficient are fixed to a constant value of 1 ($\eta_0 = \rho_0 = C_p = k = \alpha = 1$), while the gravity has been chosen as $g_y = 10^2$, in order to obtain a Rayleigh number $Ra = 10^2$. Temperatures are set to 0 on top and 1 on bottom of the domain. Velocity boundary conditions are set to free slip on all sides. The initial temperature field is given by

$$T(x, y) = (1 - y) + 0.01 \cos(\pi x) \sin(\pi y)$$

The viscosity field η is calculated as the harmonic average between a linear part η_{lin} that depends on temperature only or on temperature and depth y and a nonlinear-plastic part η_{pl} that depends on the strain rate $\dot{\epsilon}$, as follows

$$\eta(T, y, \dot{\epsilon}) = 2 \left(\frac{1}{\eta_{lin}(T, y)} + \frac{1}{\eta_{pl}(\dot{\epsilon})} \right)^{-1}$$

The linear and the nonlinear-plastic parts of the viscosity are calculated following Tosi et al. (2015) as follows

$$\begin{aligned} \eta_{lin}(T, y) &= \exp(-\ln(\Delta\eta_T)T + \ln(\Delta\eta_y)y) \\ \eta_{pl}(\dot{\epsilon}) &= \eta^* + \frac{\sigma_Y}{\sqrt{\dot{\epsilon} : \dot{\epsilon}}} \end{aligned}$$

where $\Delta\eta_T$, $\Delta\eta_y$, η^* and σ_Y are parameters chosen as listed in Table 3.

For each case, some diagnostic quantities measured at the steady state are reported in Table 4 (see Section 10.1 for the computation of all the quantities), showing a well fit with results described in Tosi et al. (2015). Data and charts for all cases can be found at https://github.com/aleregora/Benchmarks/tree/main/Momentum%2BEnergy/Viscoplastic_mantle_convection.

Case	Ra	$\Delta\eta_T$	$\Delta\eta_y$	η^*	σ_Y	Convective regime
1	10^2	10^5	1	-	-	Stagnant lid
2	10^2	10^5	1	10^{-3}	1	Mobile lid
3	10^2	10^5	10	-	-	Stagnant lid
4	10^2	10^5	10	10^{-3}	1	Mobile lid
5	10^2	10^5	10	10^{-3}	4	Periodic

Table 3: Benchmark cases and corresponding parameters.

10.21 Thin layer entrainment

This experiment is performed as originally proposed by van Keeken et al. (1997) with two incompressible fluids in a rectangular domain with $L_x = 2$ and $L_y = 1$ and gravity acceleration $g_y = 10^{10} Ra$. The Rayleigh number and the compositional Rayleigh number are fixed to $Ra = 300000$ and $Rc = 450000$, respectively. Both fluids have constant viscosity, thermal conductivity, specific heat ($\eta = \rho = C_p = 1$) and thermal expansion coefficient ($\alpha = 10^{-10}$). Fluid 1 has a density $\rho_1 = 1$, while fluid 2 is denser ($\rho_2 = \rho_1 + 1.5 \cdot 10^{-10}$) and is placed at the bottom of the domain, for $y \leq 0.025$. Temperature are set to 0 on top and 1 on bottom of the domain. Velocity boundary conditions are set to free slip on all sides of the domain. The initial temperature field is given by

$$T(x, y) = T_u(x, y) + T_l(x, y) + T_r(x, y) + T_s(x, y) - \frac{3}{2}$$

Case 1												
Code	Resolution	$\langle T \rangle$	Nu^{top}	Nu^{bottom}	v_{rms}	v_{rms}^{top}	u_{max}^{top}	η_{min}	η_{max}	$\langle W \rangle$	$\langle \Phi \rangle / Ra$	δ
YACC	100×100	0.7767	3.4298	3.3143	251.7997	1.8298	2.5516	-	-	2.4583	2.4333	1.02%
ELEFANT	100×100	0.7758	3.4214	3.313	249.134	1.8642	2.6119	-	-	2.4316	2.4276	0.16%
Stone 28	32×32	0.7737	3.3987	-	243.872	-	-	-	-	-	-	-
FALCON	100×100	0.7759	3.4280	3.3168	249.901	1.8907	2.6340	-	-	2.4299	2.4311	0.05%
Case 2												
Code	Resolution	$\langle T \rangle$	Nu^{top}	Nu^{bottom}	v_{rms}	v_{rms}^{top}	u_{max}^{top}	η_{min}	η_{max}	$\langle W \rangle$	$\langle \Phi \rangle / Ra$	δ
YACC	100×100	0.6058	8.5278	8.3990	142.2020	105.1767	122.3238	1.9853×10^{-5}	1.6095	7.6222	7.6194	0.04%
ELEFANT	100×100	0.6034	8.5115	8.4465	140.8067	104.1228	121.766	2.0600×10^{-5}	1.85	7.5665	7.5585	0.11%
Stone 28	32×32	0.6052	8.1715	-	141.518	-	-	-	-	-	-	-
FALCON	100×100	0.6044	8.5266	8.4590	141.3684	104.8867	122.0470	2.0333×10^{-5}	1.2914	7.5707	7.5718	0.01%
Case 3												
Code	Resolution	$\langle T \rangle$	Nu^{top}	Nu^{bottom}	v_{rms}	v_{rms}^{top}	u_{max}^{top}	η_{min}	η_{max}	$\langle W \rangle$	$\langle \Phi \rangle / Ra$	δ
YACC	100×100	0.7286	3.0374	2.9628	100.9467	2.0374	2.8458	4.7907×10^{-5}	1	2.0400	2.0335	0.32%
ELEFANT	100×100	0.7275	3.0347	2.9908	100.1208	2.0652	2.9019	4.8080×10^{-5}	0.9023	2.0384	2.037	0.07%
Stone 28	32×32	0.7277	3.0347	-	100.018	-	-	-	-	-	-	-
FALCON	100×100	0.7275	3.0368	3.0086	100.2776	2.0832	2.9086	4.8129×10^{-5}	0.9360	2.0387	2.0386	<0.01%
Case 4												
Code	Resolution	$\langle T \rangle$	Nu^{top}	Nu^{bottom}	v_{rms}	v_{rms}^{top}	u_{max}^{top}	η_{min}	η_{max}	$\langle W \rangle$	$\langle \Phi \rangle / Ra$	δ
YACC	100×100	0.5289	6.5572	6.5243	79.6202	75.4814	89.2940	1.9174×10^{-4}	1.6773	5.6512	5.6463	0.09%
ELEFANT	100×100	0.5277	6.5912	6.5834	79.1105	74.7596	88.9146	1.9860×10^{-4}	1.5200	5.6216	5.6182	0.06%
Stone 28	32×32	0.5286	6.4036	-	79.4746	-	-	-	-	-	-	-
FALCON	100×100	0.5279	6.5897	6.5830	79.1220	75.0715	88.8484	1.9693×10^{-4}	1.4133	5.6127	5.6113	0.03%
Case 5												
Code	Resolution	P	$\langle T \rangle_{min}$	$\langle T \rangle_{max}$	Nu_{min}^{top}	Nu_{max}^{top}	v_{rms}^{min}	v_{rms}^{max}	$(\langle \Phi \rangle / Ra)_{min}$	$(\langle \Phi \rangle / Ra)_{max}$		
YACC	100×100	0.0792	0.6543	0.6722	2.6950	7.2792	41.9813	98.8230	1.4347	9.2748		
ELEFANT	100×100	0.076	0.6514	0.6693	2.6808	7.3506	41.2578	100.089	1.3324	9.5289		
Stone 28	32×32	0.0764	0.6521	0.6697	2.6912	7.0763	41.61	98.183	-	-		
FALCON	100×100	0.0775	0.6519	0.6697	2.6847	7.3629	41.5256	99.5466	1.3399	9.3993		

Table 4: Results of the viscoplastic mantle convection benchmark for different grid resolutions in Cases 1-5 compared with results obtained with ELEFANT and YACC (100×100 elements, from [Tosi et al., 2015](#)) and in Stone 28 (32×32 elements, from https://github.com/cedrict/fieldstone/tree/master/python_codes/fieldstone_28).

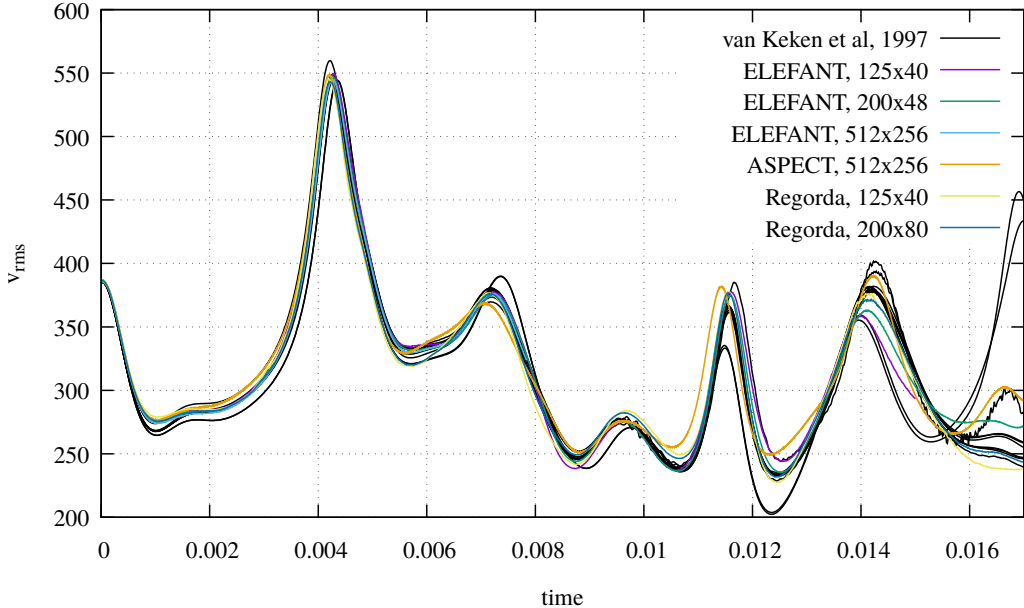


Figure 29: v_{rms} for the thin layer experiment as function of time for different grid resolution. Results are compared with results obtained by van Keken et al. (1997) (black lines) and with ASPECT and ELEFANT.

with

$$\begin{aligned} T_u(x, y) &= \frac{1}{2} \operatorname{erf} \left(\frac{1-y}{2} \sqrt{\frac{u_0}{x}} \right) \\ T_l(x, y) &= 1 - \frac{1}{2} \operatorname{erf} \left(\frac{y}{2} \sqrt{\frac{u_0}{L_x - x}} \right) \\ T_r(x, y) &= \frac{1}{2} + \frac{Q}{2\sqrt{\pi}} \sqrt{\frac{u_0}{y+1}} \exp \left(-\frac{x^2 u_0}{4y+4} \right) \\ T_s(x, y) &= \frac{1}{2} - \frac{Q}{2\sqrt{\pi}} \sqrt{\frac{u_0}{2-y}} \exp \left(-\frac{(L_x-x)^2 u_0}{8-4y} \right) \end{aligned}$$

and

$$\begin{aligned} u_0 &= \frac{L_x^{7/3}}{(1+L_x^4)^{2/3}} \left(\frac{Ra}{2\sqrt{\pi}} \right)^{\frac{2}{3}} \\ Q &= 2\sqrt{\frac{L_x}{\pi u_0}} \end{aligned}$$

The experiment is performed with two grid resolution (125×40 and 200×80 elements), with 100 markers per element and CFL of 0.25. v_{rms} (see Sec. 10.1) calculated for both the simulations match well with results from van Keken et al. (1997) and obtained with ASPECT (Kronbichler et al., 2012; Heister et al., 2017; Bangerth et al., 2020a,b) and ELEFANT (Thieulot, 2014), obtained with similar grid resolutions (Fig. 29). In addition, a variety of simulations with different resolutions and aspect ratios are performed to verify that the sensitivity of the initial velocity field. Results match well with results from van Keken et al. (1997) (in the grey area) and Thieulot (2014) (Fig. 30). All data can be found at https://github.com/aleregorde/Benchmarks/tree/main/Momentum%2BEnergy/Thin_layer.

10.22 Sinking hydrated cylinder

This experiment is performed as explained in Quinquis and Buiter (2014) and simulates the sinking of a cold, hydrated cylinder into a warm, dry mantle. The domain is square with $L_x = L_y = 300$ km, a grid resolution of 300×300 elements and 25 markers per element. The sinking cylinder is located at $x = 150$ km and $y = 170$ km with a radius of 20 km and has $\rho_c = 3250 \text{ kg m}^{-3}$, $\eta_c = 10^{23} \text{ Pa s}$, a thermal conductivity $k_c = 4.5 \text{ W m}^{-1} \text{ K}^{-1}$, a specific heat $C_{p_c} = 1250 \text{ J kg}^{-1} \text{ K}^{-1}$; the surrounding mantle has $\rho_m = 3200 \text{ kg m}^{-3}$, $\eta_m = 10^{20} \text{ Pa s}$, a thermal conductivity $k_m = 105 \text{ W m}^{-1} \text{ K}^{-1}$ and specific heat $C_{p_m} = 1250 \text{ J kg}^{-1} \text{ K}^{-1}$; a 58 km-thick lithosphere overlies the mantle and has $\rho_l = 3200 \text{ kg m}^{-3}$, $\eta_l = 10^{23} \text{ Pa s}$, a thermal conductivity $k_l = 4.5 \text{ W m}^{-1} \text{ K}^{-1}$, specific heat $C_{p_l} = 750 \text{ J kg}^{-1} \text{ K}^{-1}$ and a thermal diffusivity of $10^{-6} \text{ m}^2 \text{ s}^{-1}$. Velocity boundary conditions are set to free slip on all sides of the domain.

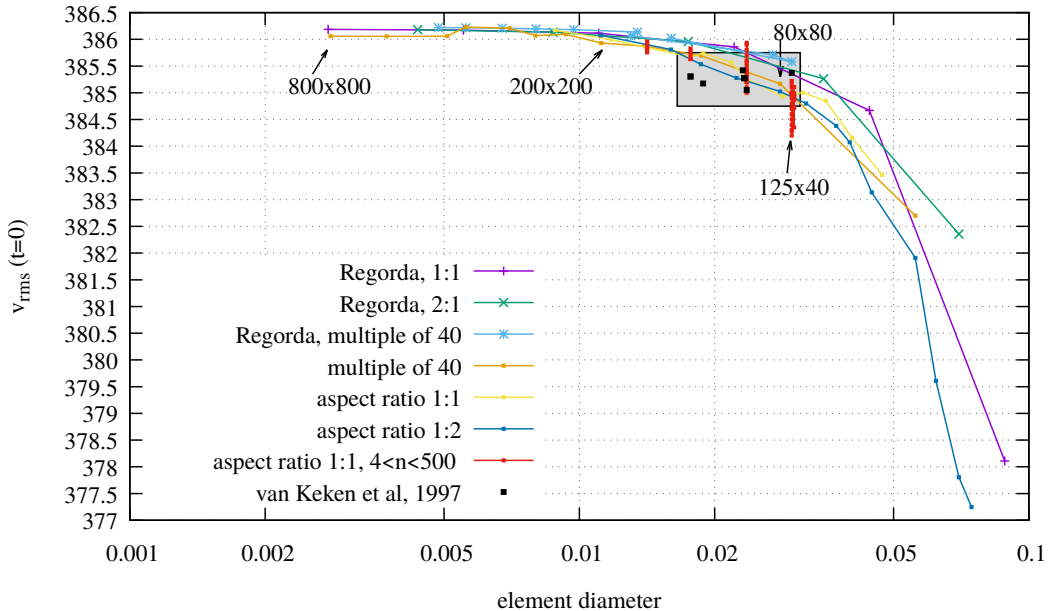


Figure 30: v_{rms} at $t = 0$ for the thin layer experiment as function of the element size for different aspect ratios of the elements. Results are compared with results obtained by van Keken et al. (1997) (black dots in the grey area) and with ASPECT and ELEFANT.

Temperature increase linearly in the lithosphere, from 0° to 1300°C , and in the mantle, from 1300° to 1360.5°C . The initial temperature of the cylinder is fixed to 400°C . Throughout the evolution, temperature is fixed to 0° and 1360.5°C at the top and bottom of the domain, respectively. The initial bound water content is imposed at 2 wt.% in the cylinder and at 0 wt.% in both the mantle and the lithosphere. The maximum amount of water in the mantle is fixed to 0.2 wt.%, while maximum water content in the cylinder and in the lithosphere is function of pressure and temperature and is calculated using a serpentinized harzburgite with Perple_X, as in Quinquis and Buiter (2014).

As shown in Quinquis and Buiter (2014), the model is characterised by a progressive dehydration in the external portion of the cylinder, due to the increase of temperature, with a consequent vertical migration of free water that hydrates the mantle above the cylinder, up to the lithosphere. The distribution of bound and free water during the evolution of the experiment is shown in Fig. 31 (left and right columns, respectively). All data can be found at <https://github.com/aleregora/Benchmarks/tree/main/Hydration>.

10.23 Mantle melting curves

This instantaneous experiment is performed in order to recreate isobaric melting curves, as function of temperature, bulk water and content of water in the melt, to compare with melting curves obtained by Katz et al. (2003). The domain is square with $L_x = L_y = 100$ km, a grid resolution of 100×100 elements and 25 markers per element. Density is set in the entire domain to 3300 kg m^{-3} and temperature increases from the sides to the centre from 1000° to 1500°C . The experiment is performed for bulk water contents from 0 to 0.3 wt.%.

Fig. 32 shows isobaric melting curves for 1 GPa (panel a) and 3 GPa (panel b) calculated for different bulk water contents. The curves well match with those obtained for the mantle by Katz et al. (2003), showing the saturation at the solidus for bulk water of 0.2 and 0.3 wt.%, indicating that the code correctly determines melt fraction as function of pressure, temperature and bulk water content. Same results can be observed in Fig. 33a, where isobaric and isothermal melting curves are shown as function of bulk water content. In addition, Fig. 33b shows that the code correctly determines also the percentage of water in the melt as function of pressure, temperature and melt fraction. All data can be found at <https://github.com/aleregora/Benchmarks/tree/main/Melting>.



Figure 31: Distribution of bound and free water (left and right columns, respectively) at $t = 0.5$ and $t = 1.25$ Myr (first and second rows, respectively) for the sinking hydrated cylinder experiment. Only markers with bound or free water not equal to 0 are plotted.



Figure 32: Isobaric melting curves for 1 GPa (panel a) and 3 GPa (panel b) as function of temperature with different bulk water contents.



Figure 33: Isobaric melting curves for 1.5 GPa as function of bulk water (panel a) and water in the melt (panel b) calculated for different temperatures.

References

- P. R. Amestoy, I. S. Duff, J.-Y. L'Excellent, and J. Koster. A fully Asynchronous Multifrontal Solver using Distributed Dynamic Scheduling. *Society for Industrial and Applied Mathematics*, 23(1):15–41, 2001.
- P. R. Amestoy, A. Buttari, J.-Y. L'Excellent, and T. Mary. Performance and Scalability of the Block Low-Rank Multifrontal Factorization on Multicore Architectures. *ACM Transactions on Mathematical Software*, 45(1):2:1–2:26, 2019.
- J. Anderson. *Computational fluid dynamics*. McGraw-Hill, 1995. ISBN 0-07-001685-2.
- D. Arcay, E. Tric, and M.-P. P. Doin. Numerical simulations of subduction zones. Effect of slab dehydration on the mantle wedge dynamics. *Physics of the Earth and Planetary Interiors*, 149(1-2 SPEC. ISS.):133–153, 2005. ISSN 00319201. doi:[10.1016/j.pepi.2004.08.020](https://doi.org/10.1016/j.pepi.2004.08.020).
- A. Y. Babeyko and S. V. Sobolev. Quantifying different modes of the late Cenozoic shortening in the central Andes. *Geology*, 33(8):621–624, 2005. ISSN 00917613. doi:[10.1130/G21126.1](https://doi.org/10.1130/G21126.1).
- W. Bangerth, J. Dannberg, R. Gassmöller, and T. Heister. Aspect v2.2.0. 2020a. doi:[10.5281/zenodo.3924604](https://doi.org/10.5281/zenodo.3924604).
- W. Bangerth, J. Dannberg, R. Gassmöller, T. Heister, et al. ASPECT: Advanced Solver for Problems in Earth's Convection, User Manual. 2020b. doi:[10.6084/m9.figshare.4865333](https://doi.org/10.6084/m9.figshare.4865333).
- R. Beucher and R. S. Huismans. Morphotectonic Evolution of Passive Margins Undergoing Active Surface Processes: Large-Scale Experiments Using Numerical Models. *Geochemistry, Geophysics, Geosystems*, 21(5), 2020. ISSN 15252027. doi:[10.1029/2019GC008884](https://doi.org/10.1029/2019GC008884).
- B. Blankenbach, F. Busse, U. Christensen, L. Cserepes, D. Gunkel, U. Hansen, H. Harder, G. Jarvis, M. Koch, G. Marquart, D. Moore, P. Olson, H. Schmeling, and T. Schnaubelt. A benchmark comparison for mantle convection codes. *Geophysical Journal International*, 98(1):23–38, 1989. ISSN 1365246X. doi:[10.1111/j.1365-246X.1989.tb05511.x](https://doi.org/10.1111/j.1365-246X.1989.tb05511.x).
- E. Burov and S. Cloetingh. Erosion and rift dynamics: New thermomechanical aspects of post-rift evolution of extensional basins. *Earth and Planetary Science Letters*, 150(1-2):7–26, 1997. ISSN 0012821X. doi:[10.1016/s0012-821x\(97\)00069-1](https://doi.org/10.1016/s0012-821x(97)00069-1).
- P. N. Chopra and M. S. Peterson. The experimental deformation of dunite. *Tectonophysics*, 78:453–473, 1981. doi:[10.1016/0040-1951\(81\)90024-X](https://doi.org/10.1016/0040-1951(81)90024-X).
- U. R. Christensen and D. A. Yuen. Layered convection induced by phase transitions. *Journal of Geophysical Research*, 90(B12):10291–10300, 1985. ISSN 01480227. doi:[10.1029/jb090ib12p10291](https://doi.org/10.1029/jb090ib12p10291).
- J. A. D. Connolly. Computation of phase equilibria by linear programming: A tool for geodynamic modeling and its application to subduction zone decarbonation. *Earth and Planetary Science Letters*, 236:524–541, 2005. doi:[10.1016/j.epsl.2005.04.033](https://doi.org/10.1016/j.epsl.2005.04.033).
- F. Crameri, P. J. Tackley, I. Meilick, T. V. Gerya, and B. J. P. Kaus. A free plate surface and weak oceanic crust produce single-sided subduction on Earth. *Geophysical Research Letters*, 39(3):1–7, 2012. ISSN 00948276. doi:[10.1029/2011GL050046](https://doi.org/10.1029/2011GL050046).
- T. Croissant and J. Braun. Constraining the stream power law: A novel approach combining a landscape evolution model and an inversion method. *Earth Surface Dynamics*, 2(1):155–166, 2014. ISSN 2196632X. doi:[10.5194/esurf-2-155-2014](https://doi.org/10.5194/esurf-2-155-2014).
- M. Dabrowski, M. Krotkiewski, and D. W. Schmid. MILAMIN: MATLAB-based finite element method solver for large problems. *Geochemistry Geophysics Geosystems*, 9(4):1–24, 2008. doi:[10.1029/2007GC001719](https://doi.org/10.1029/2007GC001719).
- J. Donea and A. Huerta. *Finite Element Methods for Flow Problems*, volume 1. Wiley, 2003. ISBN 9788578110796. doi:[10.1017/CBO9781107415324.004](https://doi.org/10.1017/CBO9781107415324.004).
- M. Faccenda. Water in the slab: A trilogy. *Tectonophysics*, 614:1–30, 2014. doi:[10.1016/j.tecto.2013.12.020](https://doi.org/10.1016/j.tecto.2013.12.020).
- M. Faccenda and N. S. Mancktelow. Fluid flow during unbending: Implications for slab hydration, intermediate-depth earthquakes and deep fluid subduction. *Tectonophysics*, 494(1-2):149–154, 2010. ISSN 00401951. doi:[10.1016/j.tecto.2010.08.002](https://doi.org/10.1016/j.tecto.2010.08.002).
- M. Faccenda, G. Minelli, and T. V. Gerya. Coupled and decoupled regimes of continental collision: Numerical modeling. *Earth and Planetary Science Letters*, 278:337–349, 2009. doi:[10.1016/j.epsl.2008.12.021](https://doi.org/10.1016/j.epsl.2008.12.021).

- M. Fraters, C. Thieulot, A. Van Den Berg, and W. Spakman. The Geodynamic World Builder: A solution for complex initial conditions in numerical modeling. *Solid Earth*, 10(5):1785–1807, 2019. ISSN 18699529. doi:[10.5194/se-10-1785-2019](https://doi.org/10.5194/se-10-1785-2019).
- T. V. Gerya. *Introduction to numerical geodynamic modelling*. Cambridge University Press, New York, 2010.
- T. V. Gerya and B. Stockhert. Exhumation rates of high pressure metamorphic rocks in subduction channels: The effect of Rheology. *Geophysical Research Letters*, 29(8):1–19, 2002. doi:[10.1029/2002TC001406](https://doi.org/10.1029/2002TC001406).
- T. V. Gerya and D. A. Yuen. Characteristics-based marker-in-cell method with conservative finite-differences schemes for modeling geological flows with strongly variable transport properties. *Physics of the Earth and Planetary Interiors*, 140:293–318, 2003. doi:[10.1016/j.pepi.2003.09.006](https://doi.org/10.1016/j.pepi.2003.09.006).
- T. V. Gerya and D. A. Yuen. Robust characteristics method for modelling multiphase visco-elasto-plastic thermo-mechanical problems. *Physics of the Earth and Planetary Interiors*, 163:83–105, 2007. doi:[10.1016/j.pepi.2007.04.015](https://doi.org/10.1016/j.pepi.2007.04.015).
- A. Glerum, C. Thieulot, M. Fraters, C. Blom, and W. Spakman. Nonlinear viscoplasticity in ASPECT: Benchmarking and applications to subduction. *Solid Earth*, 9(2):267–294, 2018. ISSN 18699529. doi:[10.5194/se-9-267-2018](https://doi.org/10.5194/se-9-267-2018).
- T. Heister, J. Dannberg, R. Gassmöller, and W. Bangerth. High accuracy mantle convection simulation through modern numerical methods. II: Realistic models and problems. *Geophysical Journal International*, 210(2):833–851, 2017. doi:[10.1093/gji/ggx195](https://doi.org/10.1093/gji/ggx195).
- G. Hirth and D. Kohlstedt. Rheology of the upper mantle and the mantle wedge: A view from the experimentalists. *Geophysical Monograph Series*, 138:83–105, 2003. ISSN 00658448. doi:[10.1029/138GM06](https://doi.org/10.1029/138GM06).
- S. Honda and M. Saito. Small-scale convection under the back arc occurring in the low viscosity wedge. *Earth and Planetary Science Letters*, 216:703–715, 2003. doi:[10.1016/S0012-821X\(03\)00537-5](https://doi.org/10.1016/S0012-821X(03)00537-5).
- S. S. Horiuchi and H. Iwamori. A consistent model for fluid distribution, viscosity distribution, and flow-thermal structure in subduction zone. *Journal of Geophysical Research: Solid Earth*, 121(5):3238–3260, 2016. ISSN 21699356. doi:[10.1002/2015JB012384](https://doi.org/10.1002/2015JB012384).
- R. S. Huismans and C. Beaumont. Symmetric and asymmetric lithospheric extension: Relative effects of frictional-plastic and viscous strain softening. *Journal of Geophysical Research: Solid Earth*, 108(B10):1–22, 2003. doi:[10.1029/2002JB002026](https://doi.org/10.1029/2002JB002026).
- R. S. Huismans, S. J. H. Buiter, and C. Beaumont. Effect of plastic-viscous layering and strain softening on mode selection during lithospheric extension. *Journal of Geophysical Research: Solid Earth*, 110(B2):1–17, 2005. doi:[10.1029/2004JB003114](https://doi.org/10.1029/2004JB003114).
- A. Ismail-Zadeh and P. Tackley. *Computational Methods for Geodynamic*. Cambridge University Press, New York, 2010. ISBN 9781626239777.
- S.-i. Karato. *Deformation of Earth Materials*. 2008. ISBN 9780521844048. doi:[10.1017/cbo9780511804892](https://doi.org/10.1017/cbo9780511804892).
- S.-i. Karato and P. Wu. Rheology of the upper mantle: A synthesis. *Science*, 260(5109):771–778, 1993. doi:[10.1126/science.260.5109.771](https://doi.org/10.1126/science.260.5109.771).
- R. F. Katz, M. Spiegelman, and C. H. Langmuir. A new parameterization of hydrous mantle melting. *Geochemistry, Geophysics, Geosystems*, 4(9):1–19, 2003. ISSN 15252027. doi:[10.1029/2002GC000433](https://doi.org/10.1029/2002GC000433).
- B. J. P. Kaus, H. Mühlhaus, and D. A. May. A stabilization algorithm for geodynamic numerical simulations with a free surface. *Physics of the Earth and Planetary Interiors*, 2010. doi:[10.1016/j.pepi.2010.04.007](https://doi.org/10.1016/j.pepi.2010.04.007).
- K. A. Kelley, T. Plank, S. Newman, E. M. Stolper, T. L. Grove, S. Parman, and E. H. Hauri. Mantle melting as a function of water content beneath the Mariana arc. *Journal of Petrology*, 51(8):1711–1738, 2010. ISSN 00223530. doi:[10.1093/petrology/egq036](https://doi.org/10.1093/petrology/egq036).
- M. Kronbichler, T. Heister, and W. Bangerth. High accuracy mantle convection simulation through modern numerical methods. *Geophysical Journal International*, 191:12–29, 2012. doi:[10.1111/j.1365-246X.2012.05609.x](https://doi.org/10.1111/j.1365-246X.2012.05609.x).
- C. H. Langmuir, A. Bézos, S. Escrig, and S. W. Parman. Chemical systematics and hydrous melting of the mantle in back-arc basins. *Geophysical Monograph Series*, 166:87–146, 2006. ISSN 23288779. doi:[10.1029/166GM07](https://doi.org/10.1029/166GM07).

- L. Liu, J. Zhang, H. W. Green, Z. Jin, and K. N. Bozhilov. Evidence of former stishovite in metamorphosed sediments, implying subduction to \sim 350 km. *Earth and Planetary Science Letters*, 263(3-4):180–191, 2007. ISSN 0012821X. doi:[10.1016/j.epsl.2007.08.010](https://doi.org/10.1016/j.epsl.2007.08.010).
- A. M. Marotta, E. Spelta, and C. Rizzetto. Gravity signature of crustal subduction inferred from numerical modelling. *Geophysical Journal International*, 166:923–938, 2006. doi:[10.1111/j.1365-246X.2006.03058.x](https://doi.org/10.1111/j.1365-246X.2006.03058.x).
- A. M. Marotta, F. Restelli, A. Bollino, A. Regorda, and R. Sabadini. The static and time-dependent signature of ocean-continent and ocean-ocean subduction: The case studies of Sumatra and Mariana complexes. *Geophysical Journal International*, 221(2):788–825, 2020. ISSN 1365246X. doi:[10.1093/gji/ggaa029](https://doi.org/10.1093/gji/ggaa029).
- M. E. Quinquis and S. J. Buitier. Testing the effects of basic numerical implementations of water migration on models of subduction dynamics. *Solid Earth*, 5(1):537–555, 2014. ISSN 1869-9529. doi:[10.5194/se-5-537-2014](https://doi.org/10.5194/se-5-537-2014).
- M. E. Quinquis, S. J. Buitier, and S. Ellis. The role of boundary conditions in numerical models of subduction zone dynamics. *Tectonophysics*, 497(1-4):57–70, 2011. ISSN 00401951. doi:[10.1016/j.tecto.2010.11.001](https://doi.org/10.1016/j.tecto.2010.11.001).
- A. Regorda, M. Roda, A. M. Marotta, and M. I. Spalla. 2-D numerical study of hydrated wedge dynamics from subduction to post-collisional phases. *Geophysical Journal International*, 211(2):974–1000, 2017. ISSN 1365246X. doi:[10.1093/gji/ggx336](https://doi.org/10.1093/gji/ggx336).
- M. Roda, A. M. Marotta, and M. I. Spalla. Influence of the thermal state of the overriding plate on the slab dip. *Rend. online Soc. Geol. It.*, 10:96–99, 2010.
- J. C. Rosas, C. A. Currie, R. N. Harris, and J. He. Effect of hydrothermal circulation on slab dehydration for the subduction zone of Costa Rica and Nicaragua. *Physics of the Earth and Planetary Interiors*, 255:66–79, 2016. ISSN 00319201. doi:[10.1016/j.pepi.2016.03.009](https://doi.org/10.1016/j.pepi.2016.03.009).
- V. Sacek, J. Braun, and P. Van Der Beek. The influence of rifting on escarpment migration on high elevation passive continental margins. *Journal of Geophysical Research: Solid Earth*, 117(4):1–18, 2012. ISSN 21699356. doi:[10.1029/2011JB008547](https://doi.org/10.1029/2011JB008547).
- S. M. Schmalholz. A simple analytical solution for slab detachment. *Earth and Planetary Science Letters*, 304(1-2):45–54, 2011. ISSN 0012821X. doi:[10.1016/j.epsl.2011.01.011](https://doi.org/10.1016/j.epsl.2011.01.011).
- H. Schmeling, A. Babeyko, A. Enns, C. Faccenna, F. Funiciello, T. Gerya, G. Golabek, S. Grigull, B. Kaus, G. Morra, S. Schmalholz, and J. van Hunen. A benchmark comparison of spontaneous subduction models—Towards a free surface. *Physics of the Earth and Planetary Interiors*, 171(1-4):198–223, 2008. ISSN 00319201. doi:[10.1016/j.pepi.2008.06.028](https://doi.org/10.1016/j.pepi.2008.06.028).
- M. W. Schmidt and S. Poli. Experimentally based water budgets for dehydrating slabs and consequences for arc magma generation. *Earth and Planetary Science Letters*, 163:361–379, 1998. doi:[10.1016/S0012-821X\(98\)00142-3](https://doi.org/10.1016/S0012-821X(98)00142-3).
- S. V. Sobolev and A. Y. Babeyko. What drives orogeny in the Andes? *Geology*, 33(8):617–620, 2005. ISSN 00917613. doi:[10.1130/G21557.1](https://doi.org/10.1130/G21557.1).
- M. Spiegelman, D. A. May, C. R. Wilson, and R. C. Wilson. On the solvability of incompressible Stokes with viscoplastic rheologies in geodynamics. *Geochemistry, Geophysics, Geosystems*, 17(6):2213–2238, 2016. ISSN 15252027. doi:[10.1002/2015GC006228](https://doi.org/10.1002/2015GC006228).
- P. J. Tackley and S. D. King. Testing the tracer ratio method for modeling active compositional fields in mantle convection simulations. *Geochemistry, Geophysics, Geosystems*, 4(4):1–15, 2003. ISSN 15252027. doi:[10.1029/2001GC000214](https://doi.org/10.1029/2001GC000214).
- C. Thieulot. FANTOM: Two- and three-dimensional numerical modelling of creeping flows for the solution of geological problems. *Physics of the Earth and Planetary Interiors*, 188(1-2):47–68, 2011. ISSN 00319201. doi:[10.1016/j.pepi.2011.06.011](https://doi.org/10.1016/j.pepi.2011.06.011).
- C. Thieulot. ELEFANT: a user-friendly multipurpose geodynamics code. *Solid Earth Discussions*, 6(2):1949–2096, 2014. ISSN 1869-9537. doi:[10.5194/sed-6-1949-2014](https://doi.org/10.5194/sed-6-1949-2014).
- C. Thieulot, P. Fullsack, and J. Braun. Adaptive octree-based finite element analysis of two- and three-dimensional indentation problems. *Journal of Geophysical Research: Solid Earth*, 113(12):1–21, 2008. ISSN 21699356. doi:[10.1029/2008JB005591](https://doi.org/10.1029/2008JB005591).
- N. Tosi, C. Stein, L. Noack, C. Hüttig, P. Maierovà, H. Samuel, D. R. Davies, C. R. Wilson, S. C. Kramer, C. Thieulot, A. Glerum, W. Spakman, A. Rozel, and P. J. Tackley. A community benchmark for viscoplastic thermal convection in a 2-D square box. *Geochemistry Geophysics Geosystems*, 16:2175–2196, 2015. doi:[10.1002/2015GC005807](https://doi.org/10.1002/2015GC005807).

- K. Ueda, S. D. Willett, T. Gerya, and J. Ruh. Geomorphological-thermo-mechanical modeling: Application to orogenic wedge dynamics. *Tectonophysics*, 659:12–30, 2015. ISSN 00401951. doi:[10.1016/j.tecto.2015.08.001](https://doi.org/10.1016/j.tecto.2015.08.001).
- P. E. van Keken, S. D. King, H. Schmeling, U. R. Christensen, D. Neumeister, and M.-P. Doin. A comparison of methods for the modeling of thermochemical convection. *Journal of Geophysical Research*, 102(B10):22477, 1997. ISSN 0148-0227. doi:[10.1029/97JB01353](https://doi.org/10.1029/97JB01353).
- H. Wang, R. Agrusta, and J. van Hunen. Advantages of a conservative velocity interpolation (cv) scheme for particle-in-cell methods with application in geodynamic modeling. *Geochemistry, Geophysics, Geosystems*, 16(6):2015–2023, 2015. doi:<https://doi.org/10.1002/2015GC005824>.
- Z. Wang, T. M. Kusky, and F. A. Capitanio. Lithosphere thinning induced by slab penetration into a hydrous mantle transition zone. *Geophysical Research Letters*, 43(22):11,567–11,577, 2016. ISSN 19448007. doi:[10.1002/2016GL071186](https://doi.org/10.1002/2016GL071186).
- C. J. Warren, C. Beaumont, and R. A. Jamieson. Deep subduction and rapid exhumation: Role of crustal strength and strain weakening in continental subduction and ultrahigh-pressure rock exhumation. *Tectonics*, 27(6):1–28, 2008. ISSN 02787407. doi:[10.1029/2008TC002292](https://doi.org/10.1029/2008TC002292).
- K. X. Whipple and G. E. Tucker. Dynamics of the stream-power river incision model: Implications for height limits of mountain ranges, landscape response timescales, and research needs. *Journal of Geophysical Research*, 104:661–674, 1999.
- S. T. Zalesak. Fully multidimensional flux-corrected transport algorithms for fluids. *Journal of Computational Physics*, 31(3):335–362, 1979. ISSN 10902716. doi:[10.1016/0021-9991\(79\)90051-2](https://doi.org/10.1016/0021-9991(79)90051-2).
- S. J. Zhong, D. A. Yuen, L. N. Moresi, and M. G. Knepley. *Numerical Methods for Mantle Convection*, volume 7. Elsevier B.V., 2015. ISBN 9780444538031. doi:[10.1016/B978-0-444-53802-4.00130-5](https://doi.org/10.1016/B978-0-444-53802-4.00130-5).